Neuronal birthdate reveals topography in a vestibular brainstem circuit for gaze stabilization

Dena Goldblatt[1,2], Stephanie Huang[1,2], Marie R. Greaney[1,3], Kyla R. Hamling[1], Venkatakaushik Voleti[4], Citlali Perez-Campos[4], Kripa B. Patel[4], Wenze Li[4], Elizabeth M. C. Hillman[4], Martha W. Bagnall[5], and David Schoppik[1]

[1]*Depts. of Otolaryngology, Neuroscience & Physiology, and the Neuroscience Institute, New York University Grossman School of Medicine, New York, NY* — [2]*Center for Neural Science, New York University, New York NY* — [3]*University of Chicago, Chicago IL* — [4]*Mortimer B. Zuckerman Mind Brain Behavior Institute, Columbia University, New York NY* — [5]*Department of Neuroscience, Washington University, St. Louis MO*

Across the nervous system, neurons with similar attributes are topographically organized. This topography reflects developmental pressures. Oddly, vestibular (balance) nuclei are thought to be disorganized. By measuring activity in birthdated neurons, we revealed a functional map within the central vestibular projection nucleus that stabilizes gaze in the larval zebrafish. We first discovered that both somatic position and stimulus selectivity follow projection neuron birthdate. Next, with electron microscopy and loss-of-function assays, we found that patterns of peripheral innervation to projection neurons were similarly organized by birthdate. Lastly, birthdate revealed spatial patterns of axonal arborization and synapse formation to projection neuron outputs. Collectively, we find that development reveals previously hidden organization to the input, processing, and output layers of a highly-conserved vertebrate sensorimotor circuit. The spatial and temporal attributes we uncover constrain the developmental mechanisms that may specify the fate, function, and organization of vestibulo-ocular reflex neurons. More broadly, our data suggest that, like invertebrates, temporal mechanisms may assemble vertebrate sensorimotor architecture.

Introduction

Neurons are often organized according to shared functional properties. Such topography exists among sensory [1–4] and motor [5–9] nuclei, reflects developmental history [10–12], and can facilitate computation [13–17]. In contrast, many brainstem nuclei appear locally disordered. One canonical example are the vestibular (balance) nuclei. While different vestibular nuclei can be coarsely distinguished by their projection targets [18–20], individual nuclei appear largely disorganized [21–25].

The apparent absence of topography is puzzling given the importance of sensory selectivity for vestibular circuit function. For example, the vertebrate vestibulo-ocular reflex uses a set of peripheral, central projection, and motor neurons (Figure 1A) to stabilize gaze after head/body movements [26]. Compensatory eye rotation behavior in the vertical axis requires stereotyped connectivity between two distinct sensory channels: one that responds exclusively to nose-up pitch-tilts and projects selectively to motor pools that rotate the eyes down, and one for the converse transformation (nose-down to eyes-up). However, no up/down organization among central vestibular projection neurons has been reported. Thus, similar to most brainstem nuclei, the organizational logic of neurons that comprise the vertical gaze stabilization circuit remains unresolved.

Developmental time organizes somatic position, circuit architecture, and neuronal function. In *Drosophila* and *C. elegans*, temporal lineage underlies neuronal cell fate [27–29], axonal connectivity [1, 30–32], and circuit membership [33, 34]. In vertebrates, neuronal birthdate is correlated with the anatomical and functional properties of neurons [30, 35–39] and circuits [40–42]. These findings suggest that ontogeny might resolve outstanding mysteries of vestibular circuit organization. The bimodal sensitivity of vertical vestibulo-ocular reflex neurons makes them an excellent model, but in mammals, their early *in utero* development constrains exploring their emergent organization.

The larval zebrafish is uniquely well-poised to explore the development of the vestibulo-ocular reflex circuit [43]. Zebrafish are vertebrates that develop externally, are optically transparent [44–47], and perform a vertical vestibulo-ocular reflex by 5 days post-fertilization [48–50]. Larvae possess both the semicircular canal and

otolithic vestibular end-organs [51, 52], stimulation of which elicits reliable responses from central projection neurons [46, 53, 54]. Prior work established that vertical (eyes-up and eyes-down) motor neurons are spatially and developmentally organized [8] and suggested that similar principles might organize the vestibular periphery [53, 55]. Whether development organizes central projection neurons – and thus the vestibulo-ocular reflex circuit – remains unclear.

Here, we characterized the anatomy and sensory selectivity of optically-birthdated [56] projection neurons. By leveraging development, we discovered somatic topography among nose-up and nose-down projection neuron subtypes. Calcium imaging, electron microscopy, and loss-of-function assays established that development organizes the vestibulo-ocular reflex circuit, from pre-synaptic peripheral inputs to post-synaptic connectivity. We conclude that development reveals the "missing" topography in the vestibular system, challenging and extending existing models of the neural architecture for balance. This topography, and the developmental pressures it may reflect, offers considerable insights into the mechanisms that may specify the fate, function, and organization of vestibulo-ocular reflex neurons. More broadly, our data support a model in which temporal forces shape the assembly and function of a complete vertebrate sensorimotor circuit.

Results

Central vestibular projection neurons are topographically organized by their birthdate

Our experiments required molecular access to projection neurons that comprise a brainstem vestibular nucleus. We used a bipartite transgenic approach consisting of a Gal4 driver line, *Tg(-6.7Tru.Hcrtr2:GAL4-VP16)* and different UAS reporter lines (Methods) to access projection neurons. Projection neurons labeled in this driver line are located in the tangential vestibular nucleus, are collectively indispensable for the vertical vestibulo-ocular reflex, and can individually and collectively induce eye rotations [50, 57]. Optical retrograde labeling [42] of projection neuron axons at their ocular motor neuron targets in cranial nucleus nIII/nIV localized their somata to a cluster at the lateral edge of rhombomeres 4-5, spanning approximately 40 μm in each spatial axis (Figure S1A-S1C). This cluster was anatomically bound ventrolaterally by the otic capsule, dorsomedially by the lateral longitudinal fasciculus, and rostrally by the lateral dendrite of the Mauthner neuron (Figure S1D-S1K). Somatic position and projection patterns are consistent with previous descriptions of the tangential vestibular nucleus [22, 58–62]. On average, we observed 37 ± 7 neurons per hemisphere (n=39 hemispheres, N=30 larvae). Our approach permits reliable access to the projection neurons in the tangential vestibular nucleus responsible for the vertical vestibulo-ocular reflex.

To define when projection neurons develop, we optically labelled neurons at distinct, experimenter-defined timepoints (Figure 1B) [56]. We then imaged "birthdated" larvae at 5 days post-fertilization (dpf) using a confocal microscope (Figure 1C). We observed a linear increase in the number of optically-tagged neurons from 22-48 hours post-fertilization (hpf) (Figure 1D), at which point the majority (92% ± 1%) of neurons were labelled (n=5 hemispheres/timepoint, 22-42 hpf; n=3 hemispheres, 48 hpf). Based on these data, we selected two temporally-defined populations for further comparative analyses: a cohort of early-born neurons born before 30 hpf (25% ± 9%), and a late-born cohort of neurons born after 48 hpf (8% ± 1%).

To determine if neuronal birthdate might reveal somatic topography, we manually registered all neurons to a common anatomical framework (Methods, Figure 1E). We discovered distinct, temporally-associated somatic organization (Figure 1F-1G). Early-born somata were exclusively observed in the dorsomedial nucleus (n=74 neurons, N=7 larvae). In contrast, late-born neurons were preferentially ventral (n=41 neurons, N=10 larvae). Spatial separation was significant across the extent of the nucleus (one-way multivariate analysis of variance, $p=5.1*10^{-14}$) and separately in the dorsoventral (two-tailed, two-sample KS test, $p=6.2*10^{-6}$) and rostrocaudal (two-tailed, two-sample KS test, p=0.02) axes. Our findings establish that neuronal birthdate predicts somatic position and reveals somatic topography within the tangential vestibular nucleus.

Birthdate predicts the functional organization of projection neurons

As birthdate anticipated soma position, we next asked if tilt sensitivity was similarly organized. Projection neurons responsible for the vertical vestibulo-ocular reflex are directionally selective and respond primarily to either nose-up or nose-down head/body tilts (Figure 2A) [63–65]. To categorize the directional selectivity of individual projection neurons, we used Tilt In Place Microscopy (TIPM) [54]. Briefly, we used a galvanometer to rotate to, and hold larvae at an eccentric angle (either 19° nose-up or nose-down). We then rapidly (~4msec) rotated the galvanometer back to horizontal, and measured the change in fluorescence of a genetically-encoded calcium indicator (GCaMP6s) (Figure 2B). As the duration of the step was orders of magnitude faster than the time constant of GCaMP6s [66], the fluorescence on return to baseline predominantly reflects neuronal activity at the previous eccentric position, and can reliably classify directional sensitivity in comparable projection neurons [54].

We categorized the subtype identity (i.e., nose-up selective / nose-down selective) of 471 projection neurons from 22 larvae. All but four neurons exhibited a transient excitatory response to at least one direction. We defined a directionality index from -1 (completely nose-down) to 1 (nose-up) and a selectivity threshold (>0.1, or ~22% difference in response magnitude, detailed in Methods). Most neurons (93%) were selective for only one direction (Figure 2C-2D; mean absolute value, nose-down: 0.73 ± 0.30; mean absolute value, nose-up: 0.84 ± 0.28). We observed a nearly equal distribution of nose-up and nose-down subtypes in our sample (44% nose-down, 49% nose-up, 7% no directional preference). Importantly, directional responses were consistent across repeated tilts (Figure 2E; mean nose-down coefficient of variation: 0.27 ± 0.21%; mean nose-up coefficient of variation: 0.39 ± 0.36%), with no variability in directional selectivity. TIPM can therefore be used to classify projection neuron subtypes. A detailed characterization of other response properties and a loss-of-function dissection of their sensory origins can be found in the Appendix.

To determine if birthdate-related topography predicted subtype identity, we performed TIPM on birthdated vestibular projection neurons (Figure 3A). Birth order predicted directional subtype preference at 5 dpf: early-born neurons almost exclusively adopted a nose-up subtype identity (n=74 neurons, N=10 larvae; 96% nose-up, 4% nose-down), while late-born neurons were predominantly nose-down (Figure 3B; n=41 neurons, N=10 larvae; 75% nose-down, 25% nose-up). To assay organization, we pseudocolored the same dataset of birthdated neurons according to their nose-up/nose-down directional preference. We observed a clear relationship between birthdate, somatic position, and subtype preference (Figure 3C). Repeated birthdating experiments at intermediate timepoints (36 hpf and 42 hpf) validated these conclusions (Supplemental Figure S4). A timecourse of projection neuron functional development can be found in the Appendix.

Early- and late-born cohorts comprise up to one-third of projection neurons. To test whether birthdated topography anticipates organization across the entire nucleus, we used a volumetric imaging approach. We performed TIPM using a swept, confocally-aligned planar excitation (SCAPE) microscope (Figure 3D-3E) [47]. Subtypes were positioned into distinct, 10 μm clusters, complementing birthdated data (Figure 3F). Specifically, nose-up neurons occupied the dorsomedial-most extent of the nucleus, while nose-down neurons clustered into two ventrolateral stripes. Finally, we tested whether we could observe organization in our full (non-birthdated) two-photon dataset (Figure 3G-3J). Spatial separation between subtypes was significant across the entire nucleus (n=360 mapped neurons, N=20 larvae; one-way multivariate analysis of variance, $p=1.1*10^{-5}$), and separately in the dorsoventral (two-tailed, two-sample KS test, $p=1.7*10^{-6}$) and mediolateral axes (two-tailed, two-sample KS test, p=0.01), and relative to chance (one-way multivariate analysis of variance, mean p=0.52 ± 0.29, details of permutation testing in Methods). A characterization of projection neuron organization according to other tilt response properties can be found in the Appendix and Supplemental Figure S5. Taken together, our data links development with function to reveal unexpected topography within a single vestibular nucleus.

Responses to high-frequency sensory stimulation are topographically organized by birthdate

Given the organization of projection neurons revealed by tonic tilt responses, we predicted that their responses to other forms of vestibular end-organ sensory stimulation – and by extension, their $VIII^{th}$ nerve sensory inputs – may be similarly organized. Projection neurons must also encode phasic (i.e. rapid) posture changes. Phasic

changes can be elicited with sufficiently high-frequency stimulation [54, 67], potentially following semicircular canal input to the tangential nucleus [22, 25, 68]. To categorize projection neurons sensitive to phasic stimuli, we performed TIPM with a stimulus consisting of two impulses of angular rotation (10 msec duration each) on the same 467 projection neurons (N=22 larvae) previously described (Figure 4A). While the responses were weaker than to tonic tilts (Figure 4B), ~60% of neurons responded significantly to impulses. Typically, neurons did not exhibit a clear preference for either impulse (Figure 4C; mean directional strength = 0.30 ± 0.26) and had little variability in response magnitude across stimulus repeats (mean coefficient of variation: 0.48 ± 0.54).

Next, we assayed if the somata of impulse-responsive projection neurons were organized in space and time. We presented impulse stimuli to the same birthdated neurons described previously (n=74 early-born neurons from N=7 larvae, n=41 late-born neurons from N=10 larvae). We observed a notable relationship between neuronal birth order and impulse responsiveness: late-born neurons were twice as likely to respond to impulses (Figure 4D; 54% responsive) than early-born (24% responsive). After registration, we observed a significant spatial separation between impulse-responsive and unresponsive neurons across the entire nucleus (one-way multivariate analysis of variance, $p=1.3*10^{-9}$). Impulse responsive neurons were restricted to the ventral (two-tailed, two-way KS test, $p=22.7*10^{-9}$), lateral (two-tailed, two-way KS test, $p=5.9*10^{-7}$), and rostral (two-tailed, two-way KS test, p=0.009) tangential vestibular nucleus (Figure 4E). We conclude that impulse-responsive projection neurons are born later and topographically constrained to the ventrolateral tangential vestibular nucleus.

Organized sensory input from semicircular canal afferents underlies the topography of high-frequency stimulation responses

The ventral localization of impulse responses allowed us to examine the nature and organization of their inputs. We predicted that impulse responsiveness might arise in part from semicircular canal afferents. To test whether the semicircular canals mediate responses to impulse stimuli, we adopted a loss-of-function approach (Appendix, Methods). We presented impulse stimuli following acute, unilateral lesions of both the anterior and posterior canal branches of the VIIIth nerve (Figure 5A). Impulse responses in ventral neurons (control: n=24 impulse responses, N=4 larvae; lesion: n=16 impulse responses, N=4 larvae) were almost entirely eliminated following canal lesions (Figure 5B; mean control dFF = 0.10 ± 0.08; mean lesion dFF = 0.05 ± 0.02; one-tailed, two-sample KS test, $p=7.4*10^{-4}$). We observed a similar decrease across the entire nucleus (control: n=40 impulse responses, N=4 larvae; lesion: n=36 impulse responses, N=4 larvae; mean control dFF: 0.08 ± 0.07; mean lesion dFF: 0.03 ± 0.05; one-tailed, two-way KS test, $p=2.8*10^{-4}$). The residual responses to impulse stimulation after canal afferent lesions may reflect otolith activation (Appendix). Thus, our loss-of-function assays support a functional role for semicircular canal afferents in mediating responses to high-frequency stimulation.

We next adopted a connectomic approach to assay whether the observed impulse sensitivity of ventral neurons might reflect targeted inputs from anterior (nose-up) and posterior (nose-down) semicircular canal afferents. Using an existing set of serial electron micrographs [55], we traced afferents from 5 dpf anterior (n=6 afferents) and posterior (n=5 afferents) semicircular canal cristae across two synaptic connections: to the statoacoustic ganglion, and then to projection neurons in the tangential vestibular nucleus (n=19 neurons) (Figure 5C). We then pseudocolored projection neurons according to whether they received anterior, posterior, or no cristae input (Figure 5D). 12/19 identifiable vestibular projection neurons in the tangential nucleus (Methods) received canal input, consistent with a previous anatomical report [22]. Input from the anterior and posterior canals was tightly organized along the rostrocaudal axis. Importantly, all canal-innervated projection neurons were located in the ventralmost 20 μm of the tangential vestibular nucleus. These ventral neurons received directionally-matched input from both utricular and canal afferents (Appendix). We conclude that semicircular canal input to projection neurons is tightly organized in space, matched to utricular afferent directionality, and preferentially targeted to later-born neurons.

Axonal trajectories and synaptic connectivity to extraocular motor neurons follow development

Somatic topography, afferent input, and response properties are organized according to birthdate. We reasoned that birthdate might similarly predict spatial connectivity to downstream extraocular motor neuron targets. Previously, we identified spatiotemporal organization among the pools of extraocular motor neurons that control vertical/torsional eye movements [8]. Motor neurons in cranial nucleus nIII that innervate eyes-down muscles are exclusively located dorsally and born earlier than their eyes-up counterparts. Additionally, we established that the axons of singly-labeled projection neurons could be classified as nose-up/eyes-down based on the presence of a characteristic branch that projects to cranial nucleus nIV, which innervates the superior oblique muscle that moves the eyes down [50]. We leveraged these facts to test whether birthdate predicts the axonal organization of vestibular projection neurons.

To measure axonal organization, we birthdated projection neurons early in development (36 hpf) and then assayed the spatial extent of their axon trajectories at 3 dpf (Figure 6A-6B). In all larvae (N=3), axons from early-born (converted) somata projected exclusively along the dorsal medial longitudinal fasciculus. Photoconverted axons also contained a characteristic branch to dorsal extraocular motor neurons in nIV, showing they originate from the nose-up projection neuron subtype (Figure 6C). We conclude that the axons of early-born (i.e., nose-up) vestibular projection neurons project dorsally in the medial longitudinal fasciculus, targeting motor neurons that move the eyes down.

We then tested whether birthdate correlates with synaptic development to target eyes-up/eyes-down motor neurons. Vestibular projection neuron axons form varicosities onto motor neuron somata; these varicosities co-localize with synaptic markers [69]. To assay synaptic development, we measured the number of axo-somatic varicosities from projection neurons onto either dorsal or ventral motor neuron somata (Figure 6D-6E). Varicosities developed in three phases: initial onset (52-55 hpf), linear growth (55-78 hpf), and plateau (>78 hpf) (Figure 5F). The initial appearance of varicosities was comparable between all dorsal and ventral motor neurons. However, varicosities to dorsal motor neurons developed more rapidly and plateaued earlier (78 hpf) than to ventral motor neurons (90 hpf). Collectively, these findings reveal that somatic birthdate anticipates both axonal and synaptic assembly onto circuit-appropriate motor neuron outputs.

Discussion

Here, we show how previously hidden functional topography in the vestibular system emerges over development. Neuronal birthdating first uncovered spatial segregation between early- and late-born projection neurons. 2-photon and volumetric imaging with TIPM showed that directional selectivity to body tilts followed soma position and birthdate. We then combined loss-of-function and electron microscopy assays to show birthdate-related organization to upstream semicircular canal inputs. Lastly, we established that birthdate differentiates the time-course of axon targeting and synapse development onto downstream ocular motor neurons. Taken together, we find that development reveals organization within the vestibular brainstem, its peripheral inputs, and its motor outputs. We propose that time plays a causal role in fate determination, topographic organization, and, by extension, vestibular circuit formation. Our data suggests mechanisms for projection neuron fate specification. More broadly, our findings offer insights into how time shapes vertebrate sensorimotor circuits.

The impact of discovering spatiotemporal topography in the vestibular system

Our discovery of spatiotemporal topography relied on bringing new tools to bear on the classic question of vestibular circuit organization. Technological improvements have a long history of revealing organization in other sensory systems, from precise olfactory maps [70, 71] to the functional architecture of the visual system [72, 73]. Prior characterizations had proposed that vestibular brainstem nuclei are disorganized [18–20, 55, 74]. Instead, retrograde tracing studies across chick, zebrafish, frog, and mouse had collectively identified coarse axonal projections – e.g., to spinal or ocular motor circuits – as their primary organizational axis [18–20, 61]. Here, we used a

modern toolkit consisting of: (1) a transgenic line of zebrafish that specifically labels vestibulo-ocular reflex projection neurons [50], (2) *in vivo* birthdating [56] early in development, and (3) spatial mapping of tilt responses [54]. These tools allowed us to extend the "axonal projection" model of vestibular brainstem organization to functional channels within an individual vestibular nucleus. More broadly, our results suggest that the vestibular brainstem is organized commonly to its sensory counterparts.

Topographic maps are the scaffold on which connectivity and function are built. Consequently, other model systems have used maps to illuminate the developmental origins of neuronal fate [75], circuit assembly [32–34, 76], and function [39, 77, 78]. Relative to other "mapped" sensory systems, almost nothing is known about vestibular reflex circuit development [79]. Below, we discuss how our spatiotemporal maps illuminate how vestibulo-ocular projection neuron fate may be determined. The common temporal topography across channels of the vestibulo-ocular reflex circuit may similarly constrain its assembly. Finally, our data illustrate how principles of invertebrate circuit development in time may be implemented in vertebrate counterparts.

The importance of birthdate in specifying vestibular projection neuron fate

Fate decisions are often the first step in constructing a neural circuit and occur upstream of the molecular logic that dictates circuit connectivity, functional attributes, and behavior [32, 75, 80–82]. What mechanisms might specify binary fate (nose-up/nose-down) in vestibular projection neurons? The absence of clearly delineated boundaries between nose-up and nose-down neurons argues against a role for spatial patterning programs. Projection neuron topography is neither laminar like cortical nuclei [83, 84] nor cleanly differentiated in one spatial axis like motor nuclei [5, 7–9, 85, 86] or brainstem nuclei [18–20, 87, 88]. Although reaction-diffusion processes can produce periodic patterns in tissue [89], the structure we see is, to the best of our knowledge, incompatible with known spatial cues. Across the hindbrain, broad spatial patterning signals act as the primary architects of rhombomeric topography [19, 61, 74, 90–92]. We propose that *within* individual vestibular nuclei, the mechanisms that specify projection neuron fate lie elsewhere.

Work in comparable systems offers several additional models for binary fate choice [93], many of which are inconsistent with our data. Specifically, our data argue against models with post-mitotic implementation of stochastic choice, sister cell interactions, and lateral inhibition. One hallmark of a stochastic process is coincident appearance of subtypes, as in *Drosophila* R7 photoreceptors [94, 95]. Similarly, cells with differential fates may be the result of interactions between coincidentally-born sister cells, as seen in v2a/v2b spinal interneurons [96, 97]. Instead, we observe a clear temporal pattern to fate specification: early-born neurons are predominantly nose-up, while late-born neurons are nose-down. We can similarly eliminate a role for mutually-repressive (lateral inhibition) programs, in which local interactions between post-mitotic neurons specify fates. Such interactions establish patterned boundaries between subtypes [98] and an unequal number of neurons in each subtype [99]. We observe that nose-up and nose-down neurons are roughly clustered and present in a 1:1 ratio. Thus, although binary (nose-up/nose-down) projection neuron fates are reminiscent of post-mitotic fate decisions in other sensory systems, they do not employ the same fate specification strategies.

Instead, projection neuron fate appears to be specified sequentially. Key evidence comes from their opposing rates of fate specification (Supplemental Figure S4), where the appearance of nose-up neurons is greatest early in development and declines as nose-down probability rises. Such a competency "switch" must reflect differential molecular logic to specify fate. In the mouse optokinetic reflex circuit, directionally-selective (up/down) retinal ganglion cells employ Tbx5 in such a manner [100]. The similarities between the vestibulo-ocular reflex and optokinetic reflex circuits argue that a comparable process may instantiate vestibular projection neuron fates. Further evidence comes from the role of Fezf1 in the fate specification of on and off starburst amacrine cells in the retina [75]. Testing this hypothesis requires uncovering the transcriptional determinants of projection neuron fate. The clear temporal delineation between nose-up and nose-down channels, together with recent transcriptional analyses of vestibular neurons [101], the zebrafish hindbrain [102, 103] and lineage tracing tools [104–106], offer a basis for differential analyses of closely-related subtypes [75, 100, 107]. Looking ahead, defining the factors that instantiate projection neuron fate will be key to understand the assembly of the vestibulo-ocular reflex circuit.

Circuit assembly: first-come, first served, or firstborn, first served?

The relationship between time and fate that we observe argues against the current "reverse order" model of vestibulo-ocular reflex circuit formation. Retrograde tracing experiments in the developing chick had suggested that projection neurons do not synapse onto extraocular motor neurons until the motor neurons connect to muscles [18]. This temporal delay led to the proposal that, for the vestibulo-ocular reflex circuit, "synaptic connectivity is established in reverse order to the signaling direction," that is, from motor neuron on to muscle, followed by vestibular projection neuron on to motor neuron, and finally vestibular afferent on to vestibular projection neuron [79, 108]. Instead, we find that vestibular projection neurons synapse on to extraocular motor neurons (Figure 7) well before those motor neurons synapse on to muscles [109]. Comparative approaches [110] could resolve the question of whether the temporal differences we observe are zebrafish-specific. Together, our work rejects the current model for vestibulo-ocular reflex ontogeny.

Sensorimotor transformations require precise connectivity, and connectivity itself could therefore determine circuit assembly. For vestibulo-ocular reflex neurons, connectivity and subtype are inextricable: eyes-down motor neurons must synapse onto eyes-down muscles, and nose-up afferents must receive input from up-tuned hair cells. Thus, synapse formation – even originating from stochastic connectivity – could define subtype [111]. Importantly, however, birthdate differentiates the subtype of vestibular projection neurons [112], extraocular motor neurons [8], and sensory afferents [55] all *before* they connect to each other. Further, projection neurons and extraocular motor neuron soma differentiate coincidentally and project early, and synaptogenesis is delayed until somatic differentiation is complete across both nuclei (Figure 7). This argues that fate and assembly in the vestibulo-ocular reflex circuit follows from time, not connectivity.

Is time *deterministic* for vestibulo-ocular reflex circuit assembly? Across the entire vestibulo-ocular reflex circuit, the nose-up/eyes-down channel develops earlier than its nose-down/eyes-up counterpart (Figure 7). The different embryological origins of channel components (ear, brain, and eye) suggest that a broad signal is required to coordinate circuit assembly. Such global timing mechanisms are well-established in *Drosophila* nervous system [113, 114]. Recent profiling studies have identified temporally-specific, though spatially-broad, patterns of gene expression in vertebrates [115]. Temporal and/or spatial transplantation approaches [4, 116] offer a means to test this hypothesis. We propose that the zebrafish vestibulo-ocular reflex circuit is a powerful model to test if global timing mechanisms coordinate channel-specific synaptic assembly to enable a functional sensorimotor circuit.

Temporal influences on sensorimotor circuit development

We propose vestibulo-ocular reflex circuit development more closely resembles invertebrate circuit development than vertebrate sensorimotor circuits. For invertebrates, the molecular logic that links time, fate, and circuit-level connectivity are well-established [31–34]. There, time reflects the synchronized and sequential expression of specific transcription factor codes, pre-mitotically and independently of space [82, 117]. In vertebrates, such tight links between lineage and fate are undefined. Though relationships between time and circuit function have been demonstrated in vertebrate circuits – for example, in zebrafish locomotor circuits for swimming [42, 78, 118] – even there, fate and connectivity are thought to arise from post-mitotic spatial cues [92, 119, 120]. In our system, the rough topography but clear temporal delineation among projection neuron subtypes argues against the primacy of spatial cues in vestibulo-ocular reflex circuit assembly.

We discovered unexpected spatiotemporal organization among vestibular projection neurons, their sensory inputs, and their motor outputs. The spatial topography we observe challenges previous reports of "disorganization" among brainstem vestibular neurons, instead illustrating that balance nuclei can resemble other sensory areas. As topographic maps reflect developmental pressures, our findings illuminate the mechanisms that may govern projection neuron fate and reflex circuit assembly, a key step forward in understanding how balance circuits come to be. Finally, the contemporaneous development of vestibulo-ocular reflex channels links vertebrate circuit assembly to temporal principles established in invertebrates. Though later maturation may disrupt the topography we observe in the larval zebrafish, our discoveries and inferences nevertheless illustrate how time may shape functional vertebrate sensorimotor circuits.

Materials and Methods

Fish care

All protocols and procedures involving zebrafish were approved by the New York University Langone School of Medicine Institutional Animal Care & Use Committee (IACUC). All larvae were raised at 28.5°C at a density of 20-50 larvae in 25-40 ml of buffered E3 (1mM HEPES added). Larvae used for photofill and birthdating experiments were raised in constant darkness; all other fish were raised on a standard 14/10h light/dark cycle. Larvae for experiments were between 1-5 days post-fertilization (dpf).

Transgenic lines

Experiments were conducted on the mifta-/- background to remove pigment. Photofill experiments were conducted on the *Tg(-6.7Tru.Hcrtr2:GAL4-VP16; UAS-E1b:Kaede)* background [50, 57, 121]. Photofill localization at nIII/nIV was validated with the *Tg(isl1:GFP)* line [122]. Two-photon calcium imaging experiments were performed on the *Tg(-6.7Tru.Hcrtr2:GAL4-VP16; UAS:GCaMP6s; atoh7:gap43-RFP)* background [123]. Functional birthdating experiments used larvae from the *Tg(-6.7Tru.Hcrtr2:GAL4-VP16; UAS:Kaede; UAS:GCaMP6s; atoh7:gap43-RFP)* background. SCAPE experiments used blind larvae from the *Tg(-6.7Tru.Hcrtr2:GAL4-VP16; UAS:Kaede; UAS:GCaMP6s; atoh7:gap43-RFP; lakritz^{th241})* background [124]. All larvae used were selected for brightness of fluorescence relative to siblings. Mendelian ratios were observed, supporting that selected larvae were homozygous for a given allele. To assay loss of the utricular otolith, we used the rks$^{vo66/vo66}$ *rock solo* otogelin knockout [125]. To label the VIIIth nerve, we used *Tg(-17.6isl2b:GFP)* [126].

Confocal imaging

Larvae were anesthetized in 0.2 mg/mL ethyl-3-aminobenzoic acid ethyl ester (MESAB, Sigma-Aldrich E10521, St. Louis, MO) prior to imaging except where noted. Larvae were mounted dorsal side-up (axial view) or lateral side-up (sagittal view) in 2% low-melting point agarose (Thermo Fisher Scientific 16520) in E3. Images were collected on a Zeiss LSM800 confocal microscope with a 20x water-immersion objective (Zeiss W Plan-Apochromat 20x/1.0). All imaging windows were 266x133 μm. Anatomy stacks of the tangential vestibular nucleus spanned approximately 50 μm in depth, sampled every micron. Raw image stacks were analyzed using Fiji/ImageJ [127].

Retrograde photolabeling of ascending projection neuron somata

Ascending projection neurons from the tangential vestibular nucleus were visualized using the *Tg(-6.7Tru.Hcrtr2:GAL4-VP16; UAS-E1b:Kaede)* line. Kaede is a photolabile protein that irreversibly converts from green to red with ultraviolet light [56]. To prevent background photoconversions, all larvae were raised in darkness. Photoconversions were performed using a confocal microscope (Zeiss LSM800) 5 dpf larvae were anesthetized and mounted axially in 2% low-melt agarose. Ascending projections were identified using the ascending bundle of axonal arbors off the medial longitudinal fasciculus at nIII/nIV [50]. Localization was validated in separate experiments on the Tg(isl1:GFP) background, which labels nIII and nIV ocular motor neurons [122]. An imaging window was centered on a single hemisphere over the midbrain-hindbrain boundary between nIII and nIV, just lateral to the medial longitudinal fasciculus. The area was repeatedly scanned with a 405 nm laser for 20-30 seconds until fully converted. Immediately after, the same plane was imaged to assess for off-target photoconversion (e.g., conversion of axonal bundles lateral to the medial longitudinal fasciculus). Larvae were unmounted and left to recover in E3 in darkness for approximately four hours to permit converted (red) Kaede to retrogradely diffuse to the somata. Photofilled fish were then re-anesthetized and mounted laterally and then axially. An imaging window was centered over hindbrain rhombomeres 4-6. Photofilled somata were identifiable by their center-surround fluorescence appearance: red converted cytoplasm, surrounding a green unconverted nucleus. Retrograde photolabeling experiments were performed in N=3 larvae.

Optical tagging of neurons by birthdate

Neuronal somata and axons were optically tagged by their time of terminal differentiation using Kaede [56]. All larvae were raised in darkness to prevent background photoconversion. Whole embryos were photoconverted for five minutes at experimenter-defined timepoints. Photoconversions were performed using a custom-built apparatus with a 405 nm LED bulb. At 5 dpf, anesthetized larvae were imaged on a confocal microscope. Only neurons born before the time of photoconversion contained converted (red) Kaede. These neurons sometimes also contained unconverted (green) Kaede, reflecting the continued production of new Kaede protein between the time of conversion and the time of imaging. Neurons that were born after the time of conversion contained only green (unconverted) Kaede. For each experiment, basal conversion was estimated by imaging control larvae raised in darkness until confocal imaging. Conversion was not observed in these larvae.

Somatic birthdating experiments

Whole embryos were birthdated at an experimenter-defined developmental stage: 22, 24, 28, 30, 33, 36, 42, or 48 hpf. Each embryo was converted at only one timepoint. n=5 hemispheres from at least N=3 separate larvae were analyzed for each timepoint between 22-42 hpf, and n=3 hemispheres from N=3 larvae were analyzed for the 48 hpf timepoint. For each timepoint, we quantified the ratio of the number of converted neurons to the total number of neurons in that hemisphere.

Spatial registration of imaged neurons

All imaged neurons were manually registered to a reference coordinate framework in Adobe Illustrator (2021). The reference framework was generated from the maximum intensity projections (MIPs) of three retrogradely-photofilled tangential vestibular nuclei, imaged on a confocal microscope. MIPs were aligned using stereotyped anatomical landmarks such as the Mauthner neuron cell body, the medial longitudinal fasciculus, and the otic capsule. MIPs for all anatomical image stacks were manually registered to this reference framework. To control for potential bias in manual registration, all registrations were verified by two independent observers (D.G. and S.H.). To control for differences in digital magnification across microscopes and larvae, all stacks were uniformly scaled to the resolution of the reference stacks (4.8 pixels/ μm).

Empirically, we observed that projection neuron somata were ~5 μm in diameter. To simplify localization, each anatomical image stack was uniformly subdivided into eight, 5 μm thick (dorsoventral) planes, such that each neuron would appear in no more than two planes. Subdivisions were assessed for consistency using distinct anatomical landmarks. Ventral planes (z3-z5) always included the Mauthner cell body. The dorsoventral midpoint (z4-z5) appeared in the same plane as the mediolateral midpoint: dorsal neurons were exclusively medial to the midpoint, and ventral neurons were exclusively lateral. The dorsomedial-most neurons in the core of the nucleus were always present in the second-most dorsal plane (z7). All subdivisions were verified by two independent observers (D.G. and S.H.). Each dorsoventral subdivision was manually registered to the MIP for that nucleus.

Neurons were manually localized to a dorsoventral subdivision based on the plane in which the soma fluorescence was brightest (soma center). Reference neurons, represented as circles approximately the diameter of a neuron, were centered over the soma in the appropriate subdivision in Illustrator. The dorsoventral subdivision and the rostrocaudal (X) and mediolateral (Y) Illustrator coordinates were manually recorded for each neuron. For standardization, their XY coordinates were normalized by subtraction from an absolute (0,0) point. This point was defined as the upper left corner of a rectangular bound, which was drawn over the extent of the photofilled tangential vestibular nucleus. Standardized coordinates were then used to recreate a spatial map of neurons imaged across all fish in Matlab (R2020b), and to link a given neuron's spatial coordinates with its functional properties. 363/467 imaged neurons were mapped.

Statistical analysis of spatial organization

Spatial organization was evaluated in two ways: i) across the entire tangential vestibular nucleus, and ii) with respect to each spatial axis separately. Global organization (three-dimensional coordinates) was evaluated using

a one-way, multivariate analysis of variance test. Organization in each individual axis was evaluated using a two-tailed, two-way Kolmogorov-Smirnov (KS) test. Marginal probability distributions of spatial localization were generated as kernel density plots using the default settings of the scatterhist Matlab function. To assess whether spatial organization was due to chance, we randomly permuted the feature of interest (e.g., up/down subtype) for all neurons while preserving the observed occurence of that feature and spatial coordinates. 100 permuted distributions were generated and statistical analyses repeated. No significant effect was ever observed in permuted distributions.

Qualitatively, we observed that the spatial separation between nose-up/nose-down subtypes was clearest in a pseudo-sagittal view of the tangential vestibular nucleus, though all confocal and two-photon images were acquired in an axial view. To determine the optimal sagittal view, we tested a set of affine transformations. 26,571 combinations of azimuth and elevation values were tested. The optimal combination (azimuth = -26.7, elevation = 51.9) was defined as that which maximized the spatial separation between nose-up and nose-down subtypes across all three spatial axes, per two-way KS tests. All reconstructions of birthdated and two-photon neuron soma position are shown as affine-transformed coordinates. All statistical analyses were performed on raw (non-transformed) coordinates.

Tonic and impulse pitch-tilt stimuli

All experiments were performed on 5 dpf larvae (Transgenic lines). Stimulation paradigms were presented as previously reported in [54] and are described again below. Larvae were paralyzed using bath application of 0.8 mg/mL pancuronium bromide (Sigma-Aldrich P1918, St. Louis, MO) for 8-10 minutes. Larvae were then mounted dorsal-up in 2% low-melt agarose in E3 in the center of the mirror on a large beam diameter single-axis scanning galvanometer system (ThorLabs GVS011, 10 mm 1D). The driver board was set to a mechanical position signal input factor of 0.5 V per degree, for a maximum mechanical scan angle of ±20.0°. Inputs of ±9.5 were delivered to the galvanometer to drive ±19° rotations in the pitch (up/down) axis.

Tonic pitch-tilt stimuli were delivered over a 65-second period. The stimulus began with an initial five-second baseline at a horizontal (0°) imaging plane, with the tangential vestibular nucleus in view. Subsequently, an instantaneous (4 ms) step was delivered to rotate the larvae -19°away from horizontal. This eccentric position was held for 15 seconds before delivering a (4 ms) horizontal restoration step, held again for 15 seconds. This process was then repeated for the nose-up position (+19°). Nose-down (-19°) stimuli were always presented first, followed by the nose-up (+19°) rotation. A neuron's directional response was defined as the change in GCaMP6s fluorescence in the first second of the return to horizontal. To control for presentation order effects, separate experiments with an inverted presentation order were performed on one larva (n=66 neurons). No significant differences were observed between these responses and all other neuronal responses.

Impulse rotations were delivered over a similar 65-second period. Larvae were presented with two sets of impulse stimuli. Each impulse was 10 ms in duration. The first impulse set contained a 4 ms downwards (-19°) rotation, a 2 ms hold, and a 4 ms restoration step to horizontal. The second impulse step contained a similar 4 ms rotation upwards (+19°), a 2 ms hold, and then a 4 ms restoration step. Each impulse was followed by a 30-second imaging window at horizontal. Impulse delivery was presented just before the equivalent restoration to horizontal in the tonic stimulus (20 and 50 seconds, respectively) to facilitate comparison of the impulse contribution to the tonic restoration step.

Tonic and impulse rotations were presented in alternating stimulus sets. Impulse rotations were always presented first, followed by tonic rotations. Three stimulus repeats (six total trials) were presented for each imaged plane for two-photon experiments, and ten trial sets (20 total trials) for SCAPE experiments.

Two-photon calcium imaging

Two-photon calcium imaging experiments were conducted using a 20x water immersion objective (Olympus XLUMPLFLN20xW 20x/1.0). The GCaMP6s calcium indicator was excited using an infrared laser (Spectra-Physics MaiTai HP) at 920 nm using approximately 6.1-18.8 mW of power, measured at the specimen with a

power meter (ThorLabs S130C). Stimulus imaging was conducted using ThorLabs LS 3.0 software. All experiments took place in the dark

Sighted 5 dpf larvae were paralyzed and mounted dorsal-up on a large beam diameter galvanometer as described above. Imaging windows were centered over rhombomeres 4-6 with both the tangential vestibular nucleus and the Mauthner neuron in view. In larvae on the *Tg(isl1:GFP)* background, GFP brightness oversaturated the photomultiplier tube in ventral planes. For these experiments, each hemisphere was imaged separately, and ventral planes were imaged with higher magnification (112x68 μm imaging window) than dorsal planes (148x91 μm imaging window). All other larvae were imaged using 205x127 μm imaging windows, with both hemispheres of the tangential vestibular nucleus in view.

An anatomical image stack of the tangential nucleus was acquired for each fish at 1 frame/second (5.2 μs pixel dwell time). Anatomy stacks spanned approximately 50 μm in depth, sampled every micron. These stacks were used to determine stimulus imaging planes. Efforts were made to sample the entire nucleus for each fish. Typically, this required sampling 6-10 planes, spaced 3-6 μm apart based on cell density. The brightness of the calcium indicator increased from the ventral- to dorsal-most neurons in a highly-stereotyped manner. Laser power was correspondingly adjusted for each plane, such that greater power (18.8 mW) was used for ventral planes compared to dorsal (6.1 mW) planes. To control for potential photobleaching effects, the nucleus was always sampled from the ventral to dorsal direction. All stimulus imaging experiments were performed at 3 frames/second (2.2 μs pixel dwell time). Total experiment time lasted approximately two hours per fish.

Classification and analysis of two-photon calcium responses to tonic and impulse rotations

We sampled 153 planes from 22 larvae. Sampling planes were pre-processed using Fiji/ImageJ [127]. For each plane, polygonal regions of interest (ROI) were drawn around all projection neuron somata visible in a maximum intensity projection of the first stimulus trial. To correct for minor (1-2 μm) inter-trial movement, ROI positions were manually adjusted in the XY axes. 37 planes were excluded due to excessive movement that caused more than one neuron to appear within an ROI. Raw fluorescence traces from polygon ROIs were extracted using Matlab R2020b (MathWorks, Natick, MA, USA) and normalized by ROI size to account for variation in imaging window size. A neuron's response was defined as the fluorescence values over the 15-second horizontal imaging window following an eccentric rotation.

To standardize responses across stimulus repeats, neurons, and larvae, all fluorescence responses were normalized by a baseline period. Some fluorescence responses remained elevated above baseline at the end of an imaging window; we accounted for this elevation in the following way, with post-hoc validation: The baseline for the static nose-down response was defined as the mean fluorescence value of the initial five-second horizontal imaging window for that trial. The baseline for the static nose-up response was defined as the mean fluorescence value of the last three seconds of the nose-down response. For impulse rotations, the baseline was defined as the mean fluorescence value of the five seconds immediately preceding the rotation. Change in fluorescence (dFF) was quantified by subtracting the appropriate baseline from each frame of the response and then normalizing by the appropriate baseline. To validate that using different baseline periods did not account for differential nose-up and nose-down response properties, all analyses were repeated for the n=66 neurons presented with an inverted directional rotation order. These analyses did not significantly change any conclusions.

We analyzed the calcium responses of 694 unique neurons. 120 neurons were excluded due to technical issues encountered during imaging. This included larvae becoming loose from the agarose, causing excessive, non-stimulus locked positional movement and response jitter. This also included loss of water between the specimen and the objective, which caused significant decreases in fluorescence brightness between trials due to the air/water interface. We excluded an additional 57 dorso-caudal cells located outside the spatial bounds of the nucleus, as defined from retrograde photofill experiments. This left us with 517 neurons for further analysis.

Each neuron's raw fluorescence and dFF timecourses of the tonic and impulse responses were manually inspected. Neurons exhibited one of three response patterns to tonic tilts: i) transient excitation that peaked in

the first second and then decayed, ii) recovery from suppression, which frequently increased to an above-baseline value, or iii) no response. Only transient excitation was observed in response to impulse stimuli. We manually classified each neuron's response pattern to each directional stimulus. To control for bias in manual classification, we only analyzed excitatory transients further if, for at least two trials, the mean raw fluorescence response in the first second was at least two standard deviations greater than baseline. 36 neurons produced clear excitatory transient responses with peaks below baseline, likely due to high background noise, and were excluded from further analysis. All subsequent analyses were conducted on the mean dFF response across all stimulus repeats.

We assigned a nose-up or nose-down identity based on the direction that produced stronger response. To quantify the strength of directional tuning, we defined a directionality index. The directionality index normalized the difference in dFF responses to the up and down rotations by their sum. Thus, negative directionality index values represented stronger nose-down responses (maximum of 1), positive values indicated stronger nose-up responses (minumum of -1), and a value of zero indicated equal nose-up and nose-down responses. To distinguish neurons with a clear directional preference from those with no preference, we set a qualitative threshold at 0.1, which represents a 22% or greater difference in relative response strength. All conclusions remained constant when eliminating or doubling this threshold. Here, 10 neurons were excluded because they produced inconsistent directional responses across stimulus repeats.

We quantified several additional response properties. The coefficient of variation across stimulus repeats was quantified as a ratio of the mean dFF response across stimulus repeats to their standard deviation. Response strength was quantified using two metrics: the mean and integral of the dFF response in the first second after the return to horizontal. The integral was estimated using the trapezoidal method with unit spacing. Response mean and integral were highly correlated ($r=0.9971$; $p<0.001$); therefore, only response mean was used for further analyses. Neuron response strength was illustrated by normalizing each neuron's mean dFF response against the maximum dFF response observed for that subtype. Lastly, to estimate the proportion of the tonic response that may originate from the rapid (4 ms) restoration step, we subtracted the impulse dFF response from the tonic dFF response to generate a "residual." To calculate the fraction of the tonic response that may be explained by the impulse step, we quantified the ratio of the residual response to the original tonic response. Lastly, some neurons exhibited slight directional tuning to impulse rotations (mean directional strength = 0.30 ± 0.26). Therefore, impulse responses to each impulse set (up/down, then down/up) were analyzed separately.

Otogelin mutant imaging and analysis

Experiments were performed on sighted 5 dpf larvae (Transgenic lines). Null otogelin mutants and sibling controls (non-phenotypic) were identified by the absence or presence of the utricular otoliths, respectively, at 5 dpf. Stimuli were delivered to three null mutants and three sibling controls under a two-photon microscope as previously described. Projection neuron responses were analyzed as previously described. 11 neurons (mutant: n=3 neurons; control: n=8 neurons) were excluded due to technical issues in imaging, leaving 183 neurons from null mutants and 144 neurons from sibling controls for further analysis (n=63±9 neurons per mutant fish, n=54±2 neurons per sibling fish, across both hemispheres). All neurons were analyzed, regardless of whether they exhibited a significant response to either stimulus. Responses were quantified as the distribution of the maximum change in fluorescence to the preferred (tonic) direction. Significant differences between the null and control distributions were assessed using a two-way, one-tailed KS test.

VIIIth nerve lesions, imaging, and analysis

Experiments were performed on a two-photon microscope using sighted 5 dpf larvae (Transgenic lines). Projection neurons were imaged before and after uni-lateral lesions of both the anterior and posterior semicircular canal branches of the VIIIth nerve. To obtain a pre-lesion baseline, paralyzed larvae were mounted dorsal-up (axially) and presented with tonic and impulse stimuli as described previously. Larvae were then re-mounted lateral side-up (sagittally) to visualize the VIIIth nerve. Lesions were targeted to the anterior and posterior semicircular canal branches of the VIIIth nerve, approximately 20-30 μm from the cristae. Lesions were performed using a pulsed in-

frared laser (SpectraPhysics Spirit 8W) at 1040 nm (400 fs pulse duration, 4 pulses per cell over 10 ms) at 25-75 nJ per pulse. Larvae were immediately imaged to confirm the extent of the lesion. Larvae were left to recover for ten minutes, re-mounted axially, and then imaged again following tonic and impulse stimuli presentation.

Neurons were only analyzed if they were identifiable in both pre- and post-lesion imaging. This left us with 62 control neurons (N=4 larvae) and 56 lesioned neurons (N=4 larvae). For impulse response analyses, neurons were only analyzed if they were impulse-responsive in the pre-lesion imaging condition (n=29 control neurons, n=33 lesioned neurons). Analyses were performed on the maximum change in fluorescence in the first second of the response following tonic and impulse rotations. All statistical analyses were conducted using a one-tailed, two-way KS test.

Functional birthdating

Experiments were performed on sighted larvae (Transgenic lines). Embryos were birthdated at 30, 36, 42, or 48 hpf as previously described. At 4 dpf, larvae were imaged on a confocal microscope to identify neurons that were born by the time of photoconversion (red, converted Kaede; early-born) or born after the time of photoconversion (green, unconverted Kaede only; late-born). Notably, late-born (green Kaede) neurons were clearly distinguishable from GCaMP6s-positive neurons given the differential localization of each fluorophore (whole-cell vs. nucleus-excluded, respectively). To avoid possible effects of an anesthetic on subsequent measures of calcium activity, larvae were not anesthetized for confocal imaging. We validated that the spatial distributions of projection neurons were constant between 4 dpf and 5 dpf by mapping neurons from five non-birthdated reference stacks from each age. No significant differences were observed between these distributions. Larvae were left to recover overnight in E3 in normal light/dark conditions.

Two-photon calcium imaging was performed at 5 dpf on paralyzed larvae. To spectrally separate green GCaMP6s from unconverted (green) Kaede, larvae were photoconverted for five minutes on our 405 nm LED apparatus to ubiquitously convert all Kaede to red. Tonic and impulse rotations were presented as previously described. Two channels (green and red) were imaged to facilitate localization of Kaede-positive neurons. Only Kaede-positive neurons were analyzed further. We manually registered the confocal stack for each imaged hemisphere to our reference framework as previously described. The coordinates and birth status (born before/born after the time of conversion) were recorded for each neuron. Neurons were then identified in the appropriate sampled stimulus plane. This permitted alignment of a given neuron's spatiotemporal developmental properties with its functional identity and rotation response features. We analyzed a total of n=74 neurons from N=10 larvae birthdated at 30 hpf; n=376 neurons from N=7 larvae birthdated at 36 hpf; n=264 neurons from N=5 larvae birthdated at 42 hpf; and n=41 neurons from N=10 larvae birthdated at 48 hpf.

Swept, confocally-aligned planar excitation (SCAPE) calcium imaging and analysis

Volumetric calcium imaging experiments were performed using a custom-built SCAPE 2.0 microscope design [47] with a 20x water immersion objective (Olympus XLUMPLFLN20xW 20x/1.0). Experiments were performed on blind 5 dpf larvae (Transgenic Lines). Paralyzed larvae were mounted dorsal-up (axial) on a large beam diameter galvanometer and imaged in an oblique (approximately 26°) coronal view. A 179x896 μm imaging window was centered over the tangential vestibular nucleus. Each volume spanned approximately 50 μm in the rostrocaudal axis, sampled every 3 μm. The rostral- and caudal-most extent was identified using the facial nucleus (nVII) and the Mauthner neuron, respectively. A high-resolution anatomical image stack was acquired at a rate of approximately 1 frame/second (0.0066 volumes per second), while stimulus imaging was performed at a rate of approximately 130 frames/second (5 volumes per second).

Larvae were presented with ten stimulus repeats (20 total trials) of the tonic and impulse stimuli as previously described. Two modifications were made to this stimulus: i) the initial baseline imaging period was extended to 15 seconds, and ii) nose-up and nose-down tilt presentation order was randomized each trial. The total experiment time per fish was approximately one hour. A second high-resolution anatomical image stack was acquired after stimulus imaging to assess for photobleaching effects. No significant photobleaching was observed.

SCAPE images were analyzed on a per-pixel basis. For each pixel, we computed the mean change in fluorescence of the first second (5 volumes) of each stimulus response relative to the initial 15-second baseline period for a given trial. The mean change in fluorescence was averaged across all ten stimulus repeats for the tonic and impulse stimuli separately. A directionality index was computed as previously described. Each pixel was then pseudo-colored according to the direction that evoked the greater change in fluorescence, as determined by the directionality index. Color intensity was scaled such that the maximum intensity corresponded to the maximum directionality index value for that subtype.

To mirror the sagittal orientation of the two-photon and confocal datasets, SCAPE images were rotated 90°around the Y-axis with interpolation. To correct the oblique angle of the SCAPE laser, an affine transformation was performed using the TransformJ plugin [128] in ImageJ and the following transformation matrix:

$$\begin{bmatrix} 1 & 0 & 0 & 0 \\ 0 & 0.707 & 0 & 0 \\ 0 & -0.707 & 1 & 0 \\ 0 & 0 & 0 & 1 \end{bmatrix}$$

Electron microscopy

Serial section electron microscopy images were obtained as described [55]. Briefly, an ultrathin (60 nm) section library of the entire zebrafish head was initially imaged at 18.8x18.8x60 nm^3 per voxel and 56.4x56.4x60 nm^3 per voxel. All myelinated axons, including those from utricular and semicircular canal afferents, were reconstructed [129]. A volume on the right side of the head, including the utricular hair cells, afferents, and most of the vestibular brainstem, was later reimaged at 4.0 × 4.0 × 60 nm^3 per voxel, allowing identification of synaptic contacts between vestibular afferents and their brainstem targets.

Projection neurons of the tangential nucleus were identified by three criteria: soma position caudal to the vestibular nerve; axonal projections that cross the midline and begin to ascend [49]; and the presence of synaptic contacts from either utricular or canal afferents. Several putative projection neurons are not included here because their axons, which exit the high-resolution reimaged territory, could not be followed adequately; these neurons are described elsewhere [130]. Therefore, the dataset is biased towards early-myelinated tangential neurons.

Each projection neuron, utricular afferent, and canal afferent was reconstructed as fully as possible. Canal afferents exited the high-resolution reimaged volume, and therefore could only be fully reconstructed if they were myelinated, whereas all utricular afferents were reconstructed. Onto projection neurons, there were no contacts from horizontal (medial) canal afferents, 89 synaptic contacts from anterior or posterior canal afferents, and 104 contacts from utricular afferents. Directional tuning of canal afferents was assumed based on canal identity (anterior canal: nose down; posterior canal: nose up). Directional tuning of utricular afferents was computed as a weighted vector sum of the hair cells forming ribbon synapses with each afferent [55].

Axon birthdating

Birthdating was performed as previously described. Whole embryos were converted at 36 hpf. At 3 dpf, anesthetized larvae were mounted lateral side-up (sagitally) to facilitate visualization of the dorsoventral separation between axon tracts. Axons were identified as dorsal-projecting based on location in the medial longitudinal fasciculus, and if they exhibited the characteristic bundle of axonal arbors off of nIV [50]. We analyzed at least one hemisphere from three separate larvae.

Quantification of post-synaptic axonal varicosity growth

Axo-somatic varicosities were quantified as a proxy for synapses [69]. Motor neuron soma were classified as dorsal or ventral based on their position relative to the appearance of nIV [8]. Anesthetized larvae were mounted dorsal-up and imaged on a confocal microscope between 50-90 hpf. Larvae were imaged no more than three times to minimize photobleaching. Varicosities were qualitatively defined as 1 μm axo-somatic spheres. We observed approximately three times as many varicosities onto all dorsal motor neurons than to ventral neurons, in line with

the differential densities of nIII and nIV [8]. Therefore, for each timepoint, varicosity growth was quantified as a percentage of the mean number of varicosities observed at 90 hpf.

Appendix

Functional responses and organization of projection neurons to tonic pitch-tilts

We used TIPM to characterize the functional response properties of projection neurons to tonic pitch-tilt rotations. We observed differences in the strength and kinetics of tilt responses between nose-up and nose-down subtypes. Nose-down neurons produced stronger calcium responses to 19° pitch-tilts than nose-up neurons (one-tailed, two-way KS test, $p=6.5*10^{-7}$; mean nose-down dFF: 1.97 ± 1.65; mean nose-up dFF: 1.21 ± 1.10) and responded to non-preferred directional stimuli with weak, transient excitation (55% of nose-down neurons). Nose-up neurons primarily responded to non-preferred directional stimuli with suppression, followed by above-baseline recovery (61% of nose-up neurons; classification detailed in Methods). This may reflect different sources of sensory input to nose-up and nose-down neurons or intrinsic differences in their encoding properties.

Projection neurons with common tilt responses were spatially clustered (Figure S5). Neurons that exhibited suppression to non-preferred directional stimuli were dorsomedially localized, while neurons with weak excitation to non-preferred directions were ventrolateral (Figure S5A). Qualitatively, we also observed spatial similarities to the soma position of neurons with similar response strengths to 19°tilts (Figure S5B). As both of these features (non-preferred response type and tilt response strength) tightly correlate with nose-up or nose-down selectivity, we propose that binary up/down subtype is the simplest axis with which to study the topography of the tangential vestibular nucleus.

Projection neuron responses to tilt stimuli originate predominantly from the utricular otoliths and secondarily from the semicircular canals

Vertical vestibular sensation is encoded by two different end organs in the inner ear: the utricular otoliths and the anterior/posterior semicircular canals. We adopted a loss-of-function approach to differentiate the contribution of each set of end-organs to our observed responses (Figure S2A). To assay the extent of the response that derived from the utricular otoliths, we presented pitch-tilt rotations to larvae with mutations in the *otogelin* gene [125]. *Otogelin* is expressed selectively in the inner ear [131]. Null *otogelin* mutants fail to develop utricular otoliths in the first two weeks, while heterozygous siblings are morphologically (Figure S2B) and functionally intact [132]. Projection neurons in *otogelin* mutants (n=183 neurons, N=3 larvae) exhibited significantly weaker calcium responses to pitch-tilt rotations compared to sibling controls (n=144 neurons, N=3 larvae; mean control dFF: 1.31 ± 1.21; mean mutant dFF: 0.36 ± 0.43; one-tailed, two-way KS test, $p=3.6*10^{-16}$) (Figure S2C) To assay the contribution of the semicircular canals, we performed acute, unilateral lesions of both the anterior and posterior canal branches of the VIIIth nerve (Figure S2D-E) We observed weaker pitch-tilt responses in projection neurons in lesioned hemispheres (n=49 neurons, n=4 larvae) compared to control hemispheres (n=57 neurons,n=4 larvae; mean control dFF = 0.89 ± 0.63; mean lesioned dFF = 0.67 ± 0.71; one-tailed, two-way KS test, $p=5.2*10^{-4}$) (Figure S2F). Thus, as expected, the observed pitch-tilt responses originate in the inner ear, predominantly from the utricular otoliths and secondarily from the semicircular canals.

Impulse responses contribute minimally to the tonic tilt response

We used impulse rotations to explore the contribution of the rapid (4 ms) restoration step in our tonic tilt stimulus. We interleaved impulse stimuli with tonic pitch-tilts and estimated the fraction of the tonic response that derived from impulse sensitivity (Figure S2A). We observed that the magnitude of the impulse response was considerably smaller than the response to the tonic stimulus (mean: 33 ± 28%). Nearly all neurons (84%) without a directional preference had an impulse response. Consistent with the ventral location of nose-down subtypes, impulse responses were more commonly observed in nose-down neurons (50% of all nose-down) than nose-up neurons (23% of all nose-up). Directional (up/down) subtype preference never changed when controlling for impulse responses, and the spatial organization of tonic nose-up/nose-down subtypes remained constant when controlling for neurons with large (≥ 10% of total) impulse responses (n=157 excluded neurons) across the entire nucleus (one-way multivariate analysis of variance, $p=8.5*10^{-9}$) and in the dorsoventral axis (two-tailed, two-sample KS

test, $p=1.9*10^{-5}$). Spatial separation became more clear in the mediolateral axis (two-tailed, two-sample KS test, p=0.005) and became significant in the rostrocaudal axis (two-tailed, two-sample KS test, p=0.008) (Figure S2B-S2C). We conclude that the observed weak, transient excitation of some neurons – in particular, nose-down subtypes – in non-preferred directions (Figure 2D) is an artifact of the rapid restoration to horizontal. Taken together, our analysis of impulse responses supports our earlier observations of spatial and temporal organization among projection neurons in the tangential nucleus.

Otolithic contributions to the impulse response

To test the possibility that impulse stimuli activate the utricular otoliths, we presented impulse stimuli to *otogelin* null larvae that are born without a utricle. Impulse responses decreased, but were not entirely eliminated, in ventral neurons on the *otogelin* background (control: n=43 impulse responses, N=3 larvae; mutant: n=33 impulse responses, N=3 larvae; mean control dFF: 0.38 ± 0.22; mean mutant dFF: 0.14 ± 0.10; one-tailed, two-way KS test, $p=1.7*10^{-7}$). We observed a similar effect to responses across the entire nucleus (control: n=169 impulse responses, N=3 larvae; mutant: n=129 impulse responses, N=3 larvae; mean control dFF: 0.25 ± 0.22; mean mutant dFF: 0.05 ± 0.08; one-tailed, two-way KS test, $p=3.0*10^{-22}$). Together, these experiments support a primary role for the semicircular canals in mediating impulse stimuli responses, with a nominal additional contribution from the utricular otoliths.

Functional development of projection neuron responses to tonic tilts

For a comprehensive characterization of projection neuron development, we performed TIPM on neurons birthdated at 30, 36, 42, or 48 hpf. We first measured the emergence of directional tilt selectivity. Competency for the nose-up subtype peaked at 36 hpf, with slower but continued addition past 48 hpf (Figure S4A-B). In contrast, nearly three-quarters of neurons born after 36 hpf acquired nose-down selectivity (Figure S4C).

To test whether other functional properties emerged in time, we measured the strength of tonic tilt responses. Nose-down neurons born after 48 hpf had significantly stronger responses to tonic rotations compared to their early-born (before 36 hpf) counterparts (mean dFF early: 0.44 ± 0.34; mean dFF late: 0.90 ± 0.82; two-tailed, two-sample KS test, p=0.01). No comparable trend was evident for early- (before 30 hpf) or late-born nose-up neurons (mean dFF early: 0.73 ± 0.49; mean dFF late: 0.77 ± 0.91; two-tailed, two-sample KS test, p=0.24). Together, these patterns may reflect distinct temporal windows in which the molecular determinants of cell fate and function are maximally expressed, with 36 hpf representing a transition between fate specification windows.

Projection neurons are innervated by directionally-matched canal and utricular afferents at 5dpf

Our connectomic data is derived from a single sample taken from a developing fish. Here we asked if afferent wiring might be sampled too early in development. We reasoned that mature vestibular projection neurons should receive directionally-matched input from both canal and utricular afferents. Canal afferent directionality in the vertical axis follows from their origin: either nose-up (anterior) or nose-down (posterior. Utricular afferent directionality is derived from the orientation of their target hair cells that are located in the macula. We traced 17 utricular afferents from their macular hair cell connections to vestibular projection neurons (Table 1) and predicted the directional tuning of these afferents based on the anatomical orientation of their hair cell inputs [55]. The vertical sensitivity of utricular and semicircular canal afferents matched perfectly in all canal-innervated projection neurons in our dataset. We conclude that directionally-selective semicircular canal inputs to vestibular projection neurons are matched to their utricular counterparts, suggesting mature patterns of innervation.

Acknowledgments

Research was supported by the National Institute on Deafness and Communication Disorders of the National Institutes of Health under award numbers R00DC012775, R56DC016316, R01DC017489, and F31DC019554, and the National Institute of Neurological Disorders and Stroke under award numbers F99NS129179, T32NS086750,

UF1NS108213, and U01NS094296. The authors would like to thank Başak Sevinç and Hannah Gelnaw for assistance with fish care, and Jeremy Dasen, Claude Desplan, Robert Froemke, Michael Long, Katherine Nagel, Dan Sanes, along with the members of the Schoppik and Nagel labs for their valuable feedback and discussions.

Author Contributions

Conceptualization: DG and DS, Methodology: DG, KH, VV, CP, KP, WL, EH, MB, MG, and DS, Investigation: DG, SH, MB, Visualization: DG, Writing: DG, Editing: DS, Funding Acquisition: DG and DS, Supervision: DS.

Author Competing Interests

The authors declare no competing interests.

References

1. Gregory S. X. E. Jefferis, Elizabeth C. Marin, Reinhard F. Stocker, and Liqun Luo. Target neuron prespecification in the olfactory map of drosophila. *Nature*, 414(6860):204–208, November 2001.
2. Christoph E. Schreiner and Jeffery A. Winer. Auditory cortex mapmaking: Principles, projections, and plasticity. *Neuron*, 56(2):356–365, October 2007.
3. Reha S. Erzurumlu, Yasunori Murakami, and Filippo M. Rijli. Mapping the face in the somatosensory brainstem. *Nature Reviews Neuroscience*, 11(4):252–263, February 2010.
4. Gabrielle R. Barsh, Adam J. Isabella, and Cecilia B. Moens. Vagus motor neuron topographic map determined by parallel mechanisms of hox5 expression and time of axon initiation. *Current Biology*, 27(24):3812–3825.e3, December 2017.
5. David L. McLean, Jingyi Fan, Shin ichi Higashijima, Melina E. Hale, and Joseph R. Fetcho. A topographic map of recruitment in spinal cord. *Nature*, 446(7131):71–75, March 2007.
6. Thomas M. Jessell, Gülşen Sürmeli, and John S. Kelly. Motor neurons and the sense of place. *Neuron*, 72(3):419–424, nov 2011.
7. Ariel J Levine, Kathryn A Lewallen, and Samuel L Pfaff. Spatial organization of cortical and spinal neurons controlling motor behavior. *Current Opinion in Neurobiology*, 22(5):812–821, October 2012.
8. Marie R. Greaney, Ann E. Privorotskiy, Kristen P. D'Elia, and David Schoppik. Extraocular motoneuron pools develop along a dorsoventral axis in zebrafish, *Danio rerio*. *Journal of Comparative Neurology*, 525(1):65–78, jun 2016.
9. Silvia Arber. Organization and function of neuronal circuits controlling movement. *EMBO Molecular Medicine*, 9(3):281–284, jan 2017.
10. Richard J Weinberg. Are topographic maps fundamental to sensory processing? *Brain Research Bulletin*, 44(2):113–116, 1997.
11. Qin Shen, Yue Wang, John T Dimos, Christopher A Fasano, Timothy N Phoenix, Ihor R Lemischka, Natalia B Ivanova, Stefano Stifani, Edward E Morrisey, and Sally Temple. The timing of cortical neurogenesis is encoded within lineages of individual progenitor cells. *Nature Neuroscience*, 9(6):743–751, May 2006.
12. Fumiaki Imamura, Albert E Ayoub, Pasko Rakic, and Charles A Greer. Timing of neurogenesis is a determinant of olfactory circuitry. *Nature Neuroscience*, 14(3):331–337, February 2011.
13. Lloyd A. Jeffress. A place theory of sound localization. *Journal of Comparative and Physiological Psychology*, 41(1):35–39, 1948.
14. Eric I. Knudsen and Michael S. Brainard. Visual instruction of the neural map of auditory space in the developing optic tectum. *Science*, 253(5015):85–87, July 1991.
15. Jon H Kaas. Topographic maps are fundamental to sensory processing. *Brain Research Bulletin*, 44(2):107–112, 1997.
16. Dmitri B. Chklovskii and Alexei A. Koulakov. MAPS IN THE BRAIN: What can we learn from them? *Annual Review of Neuroscience*, 27(1):369–392, July 2004.
17. Daniel B. Turner-Evans, Kristopher T. Jensen, Saba Ali, Tyler Paterson, Arlo Sheridan, Robert P. Ray, Tanya Wolff, J. Scott Lauritzen, Gerald M. Rubin, Davi D. Bock, and Vivek Jayaraman. The neuroanatomical ultrastructure and function of a biological ring attractor. *Neuron*, 108(1):145–163.e10, October 2020.
18. Joel C. Glover. The development of vestibulo-ocular circuitry in the chicken embryo. *Journal of Physiology-Paris*, 97(1):17–25, Jan 2003.
19. Carmen Díaz, Joel C. Glover, Luis Puelles, and Jan G. Bjaalie. The relationship between hodological and cytoarchitectonic organization in the vestibular complex of the 11-day chicken embryo. *The Journal of Comparative Neurology*, 457(1):87–105, February 2003.
20. Carmen Díaz and Luis Puelles. Segmental analysis of the vestibular nerve and the efferents of the vestibular complex. *The Anatomical Record*, 302(3):472–484, May 2018.
21. V J Wilson, M Kato, B W Peterson, and R M Wylie. A single-unit analysis of the organization of deiters' nucleus. *Journal of Neurophysiology*, 30(3):603–619, May 1967.

22. Kenna D. Peusner and D.K. Morest. The neuronal architecture and topography of the nucleus vestibularis tangentialis in the late chick embryo. *Neuroscience*, 2(2):189–IN2, April 1977.
23. William K. Abend. Functional organization of the superior vestibular nucleus of the squirrel monkey. *Brain Research*, 132(1):65–84, August 1977.
24. J. David Dickman and Qian Fang. Differential central projections of vestibular afferents in pigeons. *The Journal of Comparative Neurology*, 367(1):110–131, March 1996.
25. Hans Straka, Stefan Holler, Fumiyuki Goto, Florian P. Kolb, and Edwin Gilland. Differential spatial organization of otolith signals in frog vestibular nuclei. *Journal of Neurophysiology*, 90(5):3501–3512, nov 2003.
26. J. Szentágothai. Pathways and synaptic articulation patterns connecting vestibular receptors and oculomotor nuclei. In *The Oculomotor System*, pages 205–223. Hoeber Medical Division, Harper and Row, 1964.
27. Omer Ali Bayraktar and Chris Q. Doe. Combinatorial temporal patterning in progenitors expands neural diversity. *Nature*, 498(7455):449–455, June 2013.
28. Xin Li, Ted Erclik, Claire Bertet, Zhenqing Chen, Roumen Voutev, Srinidhi Venkatesh, Javier Morante, Arzu Celik, and Claude Desplan. Temporal patterning of drosophila medulla neuroblasts controls neural fates. *Nature*, 498(7455):456–462, June 2013.
29. Lori Glenwinkel, Seth R Taylor, Kasper Langebeck-Jensen, Laura Pereira, Molly B Reilly, Manasa Basavaraju, Ibnul Rafi, Eviatar Yemini, Roger Pocock, Nenad Sestan, Marc Hammarlund, David M Miller, and Oliver Hobert. In silico analysis of the transcriptional regulatory logic of neuronal identity specification throughout the c. elegans nervous system. *eLife*, 10, June 2021.
30. E. J. Koundakjian, J. L. Appler, and L. V. Goodrich. Auditory neurons make stereotyped wiring decisions before maturation of their targets. *Journal of Neuroscience*, 27(51):14078–14088, December 2007.
31. Luis F Sullivan, Timothy L Warren, and Chris Q Doe. Temporal identity establishes columnar neuron morphology, connectivity, and function in a drosophila navigation circuit. *eLife*, 8, February 2019.
32. Julia L Meng, Yupu Wang, Robert A Carrillo, and Ellie S Heckscher. Temporal transcription factors determine circuit membership by permanently altering motor neuron-to-muscle synaptic partnerships. *eLife*, 9, May 2020.
33. Christopher C. Wreden, Julia L. Meng, Weidong Feng, Wanhao Chi, Zarion D. Marshall, and Ellie S. Heckscher. Temporal cohorts of lineage-related neurons perform analogous functions in distinct sensorimotor circuits. *Current Biology*, 27(10):1521–1528.e4, May 2017.
34. Brandon Mark, Sen-Lin Lai, Aref Arzan Zarin, Laurina Manning, Heather Q Pollington, Ashok Litwin-Kumar, Albert Cardona, James W Truman, and Chris Q Doe. A developmental framework linking neurogenesis and circuit formation in the drosophila CNS. *eLife*, 10, May 2021.
35. M. Berry, A. W. Rogers, and J. T. Eayrs. Pattern of cell migration during cortical histogenesis. *Nature*, 203(4945):591–593, August 1964.
36. Yong-Chun Yu, Ronald S. Bultje, Xiaoqun Wang, and Song-Hai Shi. Specific synapses develop preferentially among sister excitatory neurons in the neocortex. *Nature*, 458(7237):501–504, February 2009.
37. Ye Li, Hui Lu, Pei-Lin Cheng, Shaoyu Ge, Huatai Xu, Song-Hai Shi, and Yang Dan. Clonally related visual cortical neurons show similar stimulus feature selectivity. *Nature*, May 2012.
38. Stephanie Fore, Francisca Acuña-Hinrichsen, Kadir Aytac Mutlu, Ewelina Magdalena Bartoszek, Bram Serneels, Nicholas Guy Faturos, Khac Thanh Phong Chau, Mehmet Ilyas Cosacak, Carmen Diaz Verdugo, Fabrizio Palumbo, Christa Ringers, Nathalie Jurisch-Yaksi, Caghan Kizil, and Emre Yaksi. Functional properties of habenular neurons are determined by developmental stage and sequential neurogenesis. *Science Advances*, 6(36), September 2020.
39. Roman Huszár, Yunchang Zhang, Heike Blockus, and György Buzsáki. Preconfigured dynamics in the hippocampus are guided by embryonic birthdate and rate of neurogenesis. *Nature Neuroscience*, August 2022.
40. D. L. McLean and J. R. Fetcho. Spinal interneurons differentiate sequentially from those driving the fastest swimming movements in larval zebrafish to those driving the slowest ones. *Journal of Neuroscience*, 29(43):13566–13577, October 2009.
41. J. Pujol-Marti, A. Zecca, J.-P. Baudoin, A. Faucherre, K. Asakawa, K. Kawakami, and H. Lopez-Schier. Neuronal birth order identifies a dimorphic sensorineural map. *Journal of Neuroscience*, 32(9):2976–2987, February 2012.
42. Avinash Pujala and Minoru Koyama. Chronology-based architecture of descending circuits that underlie the development of locomotor repertoire after birth. *eLife*, 8, February 2019.
43. Martha W Bagnall and David Schoppik. Development of vestibular behaviors in zebrafish. *Current Opinion in Neurobiology*, 53:83–89, December 2018.
44. Gilles C .Vanwalleghem, Misha B Ahrens, and Ethan K Scott. Integrative whole-brain neuroscience in larval zebrafish. *Current Opinion in Neurobiology*, 50:136–145, June 2018.
45. Itia A. Favre-Bulle, Gilles Vanwalleghem, Michael A. Taylor, Halina Rubinsztein-Dunlop, and Ethan K. Scott. Cellular-resolution imaging of vestibular processing across the larval zebrafish brain. *Current Biology*, 28(23):3711–3722.e3, December 2018.
46. Geoffrey Migault, Thijs L. van der Plas, Hugo Trentesaux, Thomas Panier, Raphaël Candelier, Rémi Proville, Bernhard Englitz, Georges Debrégeas, and Volker Bormuth. Whole-brain calcium imaging during physiological vestibular stimulation in larval zebrafish. *Current Biology*, 28(23):3723–3735.e6, December 2018.
47. Venkatakaushik Voleti, Kripa B. Patel, Wenze Li, Citlali Perez Campos, Srinidhi Bharadwaj, Hang Yu, Caitlin Ford, Malte J. Casper, Richard Wenwei Yan, Wenxuan Liang, Chentao Wen, Koutarou D. Kimura, Kimara L. Targoff, and Elizabeth M. C.

Hillman. Real-time volumetric microscopy of in vivo dynamics and large-scale samples with SCAPE 2.0. *Nature Methods*, 16(10):1054–1062, September 2019.

48. Bruce B. Riley and Stephen J. Moorman. Development of utricular otoliths, but not saccular otoliths, is necessary for vestibular function and survival in zebrafish. *Journal of Neurobiology*, 43(4):329–337, 2000.
49. Isaac H. Bianco, Leung-Hang Ma, David Schoppik, Drew N. Robson, Michael B. Orger, James C. Beck, Jennifer M. Li, Alexander F. Schier, Florian Engert, and Robert Baker. The tangential nucleus controls a gravito-inertial vestibulo-ocular reflex. *Current Biology*, 22(14):1285–1295, Jul 2012.
50. David Schoppik, Isaac H. Bianco, David A. Prober, Adam D. Douglass, Drew N. Robson, Jennifer M.B. Li, Joel S.F. Greenwood, Edward Soucy, Florian Engert, and Alexander F. Schier. Gaze-stabilizing central vestibular neurons project asymmetrically to extraocular motoneuron pools. *The Journal of Neuroscience*, 37(47):11353–11365, sep 2017.
51. F. M. Lambert, J. C. Beck, R. Baker, and H. Straka. Semicircular canal size determines the developmental onset of angular vestibuloocular reflexes in larval xenopus. *Journal of Neuroscience*, 28(32):8086–8095, aug 2008.
52. Weike Mo, Fangyi Chen, Alex Nechiporuk, and Teresa Nicolson. Quantification of vestibular-induced eye movements in zebrafish larvae. *BMC Neuroscience*, 11(1):110, 2010.
53. Masashi Tanimoto, Ikuko Watakabe, and Shin ichi Higashijima. Tiltable objective microscope visualizes discrimination of static and dynamic head movement originates at hair cells. *bioRxiv*, July 2022.
54. Kyla R. Hamling, Yunlu Zhu, Franziska Auer, and David Schoppik. Tilt in place microscopy (TIPM): a simple, low-cost solution to image neural responses to body rotations. *bioRxiv*, September 2022.
55. Zhikai Liu, David G. C. Hildebrand, Joshua L. Morgan, Yizhen Jia, Nicholas Slimmon, and Martha W. Bagnall. Organization of the gravity-sensing system in zebrafish. *Nature Communications*, 13(1), August 2022.
56. S. J. C. Caron, D. Prober, M. Choy, and A. F. Schier. *In vivo* birthdating by BAPTISM reveals that trigeminal sensory neuron diversity depends on early neurogenesis. *Development*, 135(19):3259–3269, Aug 2008.
57. Alix M.B. Lacoste, David Schoppik, Drew N. Robson, Martin Haesemeyer, Ruben Portugues, Jennifer M. Li, Owen Randlett, Caroline L. Wee, Florian Engert, and Alexander F. Schier. A convergent and essential interneuron pathway for mauthner-cell-mediated escapes. *Current Biology*, 25(11):1526–1534, jun 2015.
58. Santiago Ramon y Cajal. Sur un noyau special du nerf vestibulaire des poissons et des oiseaux. *Trabajos del Laboratorio de Investigaciones Biolo´gicas de la Universidad de Madrid*, 6:1–20, 1908.
59. Rita Levi-montalcini. The development of the acoustico-vestibular centres in the chick embryo in the absence of the afferent root fibers and of descending fiber tracts. *The Journal of Comparative Neurology*, 91(2):209–241, October 1949.
60. Anastas Popratiloff and Kenna D. Peusner. Otolith fibers and terminals in chick vestibular nuclei. *The Journal of Comparative Neurology*, 502(1):19–37, 2007.
61. Hans Straka, Robert Baker, and Edwin Gilland. Rhombomeric organization of vestibular pathways in larval frogs. *Journal of Comparative Neurology*, 437(1):42–55, July 2001.
62. Hans Straka and Robert Baker. Vestibular blueprint in early vertebrates. *Frontiers in Neural Circuits*, 7, 2013.
63. S. M. Highstein, J. M. Goldberg, A. K. Moschovakis, and C. Fernandez. Inputs from regularly and irregularly discharging vestibular nerve afferents to secondary neurons in the vestibular nuclei of the squirrel monkey. II. correlation with output pathways of secondary neurons. *Journal of Neurophysiology*, 58(4):719–738, October 1987.
64. R. A. McCrea, A. Strassman, and S. M. Highstein. Anatomical and physiological characteristics of vestibular neurons mediating the vertical vestibulo-ocular reflexes of the squirrel monkey. *The Journal of Comparative Neurology*, 264(4):571–594, October 1987.
65. Y. Iwamoto, T. Kitama, and K. Yoshida. Vertical eye movement-related secondary vestibular neurons ascending in medial longitudinal fasciculus in cat. II. direct connections with extraocular motoneurons. *Journal of Neurophysiology*, 63(4):918–935, April 1990.
66. Tsai-Wen Chen, Trevor J. Wardill, Yi Sun, Stefan R. Pulver, Sabine L. Renninger, Amy Baohan, Eric R. Schreiter, Rex A. Kerr, Michael B. Orger, Vivek Jayaraman, Loren L. Looger, Karel Svoboda, and Douglas S. Kim. Ultrasensitive fluorescent proteins for imaging neuronal activity. *Nature*, 499(7458):295–300, July 2013.
67. Francisco Branoner and Hans Straka. Semicircular canal-dependent developmental tuning of translational vestibulo-ocular reflexes in *Xenopus laevis*. *Developmental Neurobiology*, 75(10):1051–1067, October 2014.
68. Gloria E. Meredith and Ann B. Butler. Organization of eighth nerve afferent projections from individual endorgans of the inner ear in the teleost, astronotus ocellatus. *The Journal of Comparative Neurology*, 220(1):44–62, October 1983.
69. Limor Freifeld, Iris Odstrcil, Dominique Förster, Alyson Ramirez, James A. Gagnon, Owen Randlett, Emma K. Costa, Shoh Asano, Orhan T. Celiker, Ruixuan Gao, Daniel A. Martin-Alarcon, Paul Reginato, Cortni Dick, Linlin Chen, David Schoppik, Florian Engert, Herwig Baier, and Edward S. Boyden. Expansion microscopy of zebrafish for neuroscience and developmental biology studies. *Proceedings of the National Academy of Sciences*, 114(50):E10799–E10808, nov 2017.
70. W. E. L. G. Clark. The projection of the olfactory epithilium on the olfactory bulb in the rabbit. *Journal of Neurology, Neurosurgery & Psychiatry*, 14(1):1–10, February 1951.
71. Peter Mombaerts, Fan Wang, Catherine Dulac, Steve K Chao, Adriana Nemes, Monica Mendelsohn, James Edmondson, and Richard Axel. Visualizing an olfactory sensory map. *Cell*, 87(4):675–686, November 1996.

72. G. Holmes. Disturbances of vision by cereberal lesions. *British Journal of Ophthalmology*, 2(7):353–384, July 1918.
73. D. H. Hubel and T. N. Wiesel. Receptive fields, binocular interaction and functional architecture in the cat's visual cortex. *The Journal of Physiology*, 160(1):106–154, January 1962.
74. M. Pasqualetti, C. Diaz, J.-S. Renaud, F. M. Rijli, and J. C. Glover. Fate-mapping the mammalian hindbrain: Segmental origins of vestibular projection neurons assessed using rhombomere-specific hoxa2 enhancer elements in the mouse embryo. *Journal of Neuroscience*, 27(36):9670–9681, September 2007.
75. Yi-Rong Peng, Rebecca E. James, Wenjun Yan, Jeremy N. Kay, Alex L. Kolodkin, and Joshua R. Sanes. Binary fate choice between closely related interneuronal types is determined by a fezf1-dependent postmitotic transcriptional switch. *Neuron*, 105(3):464–474.e6, February 2020.
76. Dong-Jing Zou, Paul Feinstein, Aimée L. Rivers, Glennis A. Mathews, Ann Kim, Charles A. Greer, Peter Mombaerts, and Stuart Firestein. Postnatal refinement of peripheral olfactory projections. *Science*, 304(5679):1976–1979, June 2004.
77. David H. Hubel and Torsten N. Wiesel. Binocular interaction in striate cortex of kittens reared with artificial squint. *Journal of Neurophysiology*, 28(6):1041–1059, November 1965.
78. Joseph R. Fetcho and David L. McLean. Some principles of organization of spinal neurons underlying locomotion in zebrafish and their implications. *Annals of the New York Academy of Sciences*, 1198(1):94–104, Jun 2010.
79. Mathieu Beraneck, François M. Lambert, and Soroush G. Sadeghi. Functional development of the vestibular system. In *Development of Auditory and Vestibular Systems*, pages 449–487. Elsevier, 2014.
80. Lu O. Sun, Zheng Jiang, Michal Rivlin-Etzion, Randal Hand, Colleen M. Brady, Ryota L. Matsuoka, King-Wai Yau, Marla B. Feller, and Alex L. Kolodkin. On and off retinal circuit assembly by divergent molecular mechanisms. *Science*, 342(6158), November 2013.
81. Austin Q. Seroka and Chris Q. Doe. The hunchback temporal transcription factor determines motor neuron axon and dendrite targeting in *Drosophila*. *Development*, January 2019.
82. Nikolaos Konstantinides, Isabel Holguera, Anthony M. Rossi, Aristides Escobar, Liébaut Dudragne, Yen-Chung Chen, Thinh N. Tran, Azalia M. Martínez Jaimes, Mehmet Neset Özel, Félix Simon, Zhiping Shao, Nadejda M. Tsankova, John F. Fullard, Uwe Walldorf, Panos Roussos, and Claude Desplan. A complete temporal transcription factor series in the fly visual system. *Nature*, 604(7905):316–322, April 2022.
83. Korbinian Brodmann. *Vergleichende Lokalisationslehre der Grosshirnrinde in ihren Prinzipien dargestellt auf Grund des Zellenbaues*. Barth, 1909.
84. Vernon B Mountcastle. The columnar organization of the neocortex. *Brain: a journal of neurology*, 120(4):701–722, 1997.
85. L Landmesser. The distribution of motoneurones supplying chick hind limb muscles. *The Journal of Physiology*, 284(1):371–389, November 1978.
86. L Landmesser. The development of motor projection patterns in the chick hind limb. *The Journal of Physiology*, 284(1):391–414, November 1978.
87. Maria Soledad Esposito, Paolo Capelli, and Silvia Arber. Brainstem nucleus MdV mediates skilled forelimb motor tasks. *Nature*, 508(7496):351–356, February 2014.
88. Ludwig Ruder, Riccardo Schina, Harsh Kanodia, Sara Valencia-Garcia, Chiara Pivetta, and Silvia Arber. A functional map for diverse forelimb actions within brainstem circuitry. *Nature*, 590(7846):445–450, January 2021.
89. Alan M. Turing. The chemical basis of morphogenesis. *Philosophical Transactions of the Royal Society of London. Series B, Biological Sciences*, 237(641):37–72, August 1952.
90. Cecilia B. Moens and Victoria E. Prince. Constructing the hindbrain: Insights from the zebrafish. *Developmental Dynamics*, 224(1):1–17, April 2002.
91. Stefan Tümpel, Leanne M. Wiedemann, and Robb Krumlauf. Chapter 8 hox genes and segmentation of the vertebrate hindbrain. In *Current Topics in Developmental Biology*, pages 103–137. Elsevier, 2009.
92. Amina Kinkhabwala, Michael Riley, Minoru Koyama, Joost Monen, Chie Satou, Yukiko Kimura, Shin ichi Higashijima, and Joseph Fetcho. A structural and functional ground plan for neurons in the hindbrain of zebrafish. *Proceedings of the National Academy of Sciences*, 108(3):1164–1169, January 2011.
93. David Jukam and Claude Desplan. Binary fate decisions in differentiating neurons. *Current Opinion in Neurobiology*, 20(1):6–13, February 2010.
94. Mathias F. Wernet, Esteban O. Mazzoni, Arzu Çelik, Dianne M. Duncan, Ian Duncan, and Claude Desplan. Stochastic spineless expression creates the retinal mosaic for colour vision. *Nature*, 440(7081):174–180, March 2006.
95. Lukas Voortman, Caitlin Anderson, Elizabeth Urban, Luorongxin Yuan, Sang Tran, Alexandra Neuhaus-Follini, Josh Derrick, Thomas Gregor, and Robert J. Johnston. Temporally dynamic antagonism between transcription and chromatin compaction controls stochastic photoreceptor specification in flies. *Developmental Cell*, 57(15):1817–1832.e5, August 2022.
96. Yukiko Kimura, Chie Satou, and Shin ichi Higashijima. V2a and v2b neurons are generated by the final divisions of pair-producing progenitors in the zebrafish spinal cord. *Development*, 135(18):3001–3005, September 2008.
97. Saul Bello-Rojas and Martha W. Bagnall. Clonally related, notch-differentiated spinal neurons integrate into distinct circuits. *bioRxiv*, September 2022.

98. Joanne R. Collier, Nicholas A.M. Monk, Philip K. Maini, and Julian H. Lewis. Pattern formation by lateral inhibition with feedback: a mathematical model of delta-notch intercellular signalling. *Journal of Theoretical Biology*, 183(4):429–446, December 1996.
99. Marion Langen, Marta Koch, Jiekun Yan, Natalie De Geest, Maria-Luise Erfurth, Barret D Pfeiffer, Dietmar Schmucker, Yves Moreau, and Bassem A Hassan. Mutual inhibition among postmitotic neurons regulates robustness of brain wiring in drosophila. *eLife*, 2, March 2013.
100. Timour Al-Khindi, Michael B. Sherman, Takashi Kodama, Preethi Gopal, Zhiwei Pan, James K. Kiraly, Hao Zhang, Loyal A. Goff, Sascha du Lac, and Alex L. Kolodkin. The transcription factor tbx5 regulates direction-selective retinal ganglion cell development and image stabilization. *Current Biology*, August 2022.
101. Takashi Kodama, Aryn H. Gittis, Minyoung Shin, Keith Kelleher, Kristine E. Kolkman, Lauren McElvain, Minh Lam, and Sascha du Lac. Graded coexpression of ion channel, neurofilament, and synaptic genes in fast-spiking vestibular nucleus neurons. *The Journal of Neuroscience*, 40(3):496–508, November 2019.
102. Dylan R. Farnsworth, Lauren M. Saunders, and Adam C. Miller. A single-cell transcriptome atlas for zebrafish development. *Developmental Biology*, 459(2):100–108, March 2020.
103. Monica Tambalo, Richard Mitter, and David G. Wilkinson. A single cell transcriptome atlas of the developing zebrafish hindbrain. *Development*, January 2020.
104. Jeffrey A. Farrell, Yiqun Wang, Samantha J. Riesenfeld, Karthik Shekhar, Aviv Regev, and Alexander F. Schier. Single-cell reconstruction of developmental trajectories during zebrafish embryogenesis. *Science*, 360(6392), June 2018.
105. Daniel E. Wagner, Caleb Weinreb, Zach M. Collins, James A. Briggs, Sean G. Megason, and Allon M. Klein. Single-cell mapping of gene expression landscapes and lineage in the zebrafish embryo. *Science*, 360(6392):981–987, June 2018.
106. Bushra Raj, Jeffrey A. Farrell, Jialin Liu, Jakob El Kholtei, Adam N. Carte, Joaquin Navajas Acedo, Lucia Y. Du, Aaron McKenna, Đorđe Relić, Jessica M. Leslie, and Alexander F. Schier. Emergence of neuronal diversity during vertebrate brain development. *Neuron*, 108(6):1058–1074.e6, December 2020.
107. Hongjie Li, Felix Horns, Bing Wu, Qijing Xie, Jiefu Li, Tongchao Li, David J. Luginbuhl, Stephen R. Quake, and Liqun Luo. Classifying drosophila olfactory projection neuron subtypes by single-cell RNA sequencing. *Cell*, 171(5):1206–1220.e22, November 2017.
108. Hans Straka. Ontogenetic rules and constraints of vestibulo-ocular reflex development. *Current Opinion in Neurobiology*, 20(6):689–695, December 2010.
109. C. Clark, O. Austen, I. Poparic, and S. Guthrie. α2-chimaerin regulates a key axon guidance transition during development of the oculomotor projection. *Journal of Neuroscience*, 33(42):16540–16551, Oct 2013.
110. Hans Straka, Bernd Fritzsch, and Joel C. Glover. Connecting ears to eye muscles: Evolution of a 'simple' reflex arc. *Brain, Behavior and Evolution*, 83(2):162–175, 2014.
111. Bassem A. Hassan and P. Robin Hiesinger. Beyond molecular codes: Simple rules to wire complex brains. *Cell*, 163(2):285–291, October 2015.
112. Joel C. Glover. Neuroepithelial 'compartments' and the specification of vestibular projections. In *Progress in Brain Research*, pages 3–21. Elsevier, 2000.
113. Mubarak Hussain Syed, Brandon Mark, and Chris Q Doe. Steroid hormone induction of temporal gene expression in drosophila brain neuroblasts generates neuronal and glial diversity. *eLife*, 6, April 2017.
114. Rosa Linda Miyares and Tzumin Lee. Temporal control of drosophila central nervous system development. *Current Opinion in Neurobiology*, 56:24–32, June 2019.
115. Andreas Sagner, Isabel Zhang, Thomas Watson, Jorge Lazaro, Manuela Melchionda, and James Briscoe. A shared transcriptional code orchestrates temporal patterning of the central nervous system. *PLOS Biology*, 19(11):e3001450, November 2021.
116. Adam J. Isabella, Jason A. Stonick, Julien Dubrulle, and Cecilia B. Moens. Intrinsic positional memory guides target-specific axon regeneration in the zebrafish vagus nerve. *Development*, 148(18), September 2021.
117. Chris Q. Doe. Temporal patterning in the *Drosophila* cns. *Annual Review of Cell and Developmental Biology*, 33(1):219–240, October 2017.
118. Sandeep Kishore, Eli B. Cadoff, Moneeza A. Agha, and David L. McLean. Orderly compartmental mapping of premotor inhibition in the developing zebrafish spinal cord. *Science*, 370(6515):431–436, October 2020.
119. Thomas M. Jessell. Neuronal specification in the spinal cord: inductive signals and transcriptional codes. *Nature Reviews Genetics*, 1(1):20–29, October 2000.
120. Gülşen Sürmeli, Turgay Akay, Gregory C. Ippolito, Philip W. Tucker, and Thomas M. Jessell. Patterns of spinal sensory-motor connectivity prescribed by a dorsoventral positional template. *Cell*, 147(3):653–665, October 2011.
121. Ethan K. Scott, Lindsay Mason, Aristides B. Arrenberg, Limor Ziv, Nathan J Gosse, Tong Xiao, Neil C. Chi, Kazuhide Asakawa, Koichi Kawakami, and Herwig Baier. Targeting neural circuitry in zebrafish using GAL4 enhancer trapping. *Nature Methods*, mar 2007.
122. S. Higashijima, Y. Hotta, and H. Okamoto. Visualization of cranial motor neurons in live transgenic zebrafish expressing green fluorescent protein under the control of the *Islet*-1 promoter/enhancer. *Journal of Neuroscience*, 20(1):206–218, Jan 2000.

123. Flavio R Zolessi, Lucia Poggi, Christopher J Wilkinson, Chi-Bin Chien, and William A Harris. Polarization and orientation of retinal ganglion cells *in vivo*. *Neural Development*, 1(1):2, 2006.
124. Jeremy N Kay, Karin C Finger-Baier, Tobias Roeser, Wendy Staub, and Herwig Baier. Retinal ganglion cell genesis requires lakritz, a zebrafish atonal homolog. *Neuron*, 30(3):725–736, May 2001.
125. T.T. Whitfield, M. Granato, F.J. van Eeden, U. Schach, M. Brand, M. Furutani-Seiki, P. Haffter, M. Hammerschmidt, C.P. Heisenberg, Y.J. Jiang, D.A. Kane, R.N. Kelsh, M.C. Mullins, J. Odenthal, and C. Nusslein-Volhard. Mutations affecting development of the zebrafish inner ear and lateral line. *Development*, 123(1):241–254, December 1996.
126. A. J. Pittman, M.-Y. Law, and C.-B. Chien. Pathfinding in a large vertebrate axon tract: isotypic interactions guide retinotectal axons at multiple choice points. *Development*, 135(17):2865–2871, sep 2008.
127. Johannes Schindelin, Ignacio Arganda-Carreras, Erwin Frise, Verena Kaynig, Mark Longair, Tobias Pietzsch, Stephan Preibisch, Curtis Rueden, Stephan Saalfeld, Benjamin Schmid, Jean-Yves Tinevez, Daniel James White, Volker Hartenstein, Kevin Eliceiri, Pavel Tomancak, and Albert Cardona. Fiji: an open-source platform for biological-image analysis. *Nature Methods*, 9(7):676–682, Jun 2012.
128. Erik H.W. Meijering, Wiro J. Niessen, and Max A. Viergever. Quantitative evaluation of convolution-based methods for medical image interpolation. *Medical Image Analysis*, 5(2):111–126, June 2001.
129. David Grant Colburn Hildebrand, Marcelo Cicconet, Russel Miguel Torres, Woohyuk Choi, Tran Minh Quan, Jungmin Moon, Arthur Willis Wetzel, Andrew Scott Champion, Brett Jesse Graham, Owen Randlett, George Scott Plummer, Ruben Portugues, Isaac Henry Bianco, Stephan Saalfeld, Alexander David Baden, Kunal Lillaney, Randal Burns, Joshua Tzvi Vogelstein, Alexander Franz Schier, Wei-Chung Allen Lee, Won-Ki Jeong, Jeff William Lichtman, and Florian Engert. Whole-brain serial-section electron microscopy in larval zebrafish. *Nature*, 545(7654):345–349, May 2017.
130. Yizhen Jia and Martha W. Bagnall. Monosynaptic targets of utricular afferents in the larval zebrafish. *Frontiers in Neurology*, 13, July 2022.
131. G. A. Stooke-Vaughan, N. D. Obholzer, S. Baxendale, S. G. Megason, and T. T. Whitfield. Otolith tethering in the zebrafish otic vesicle requires otogelin and -tectorin. *Development*, 142(6):1137–1145, 2015.
132. Richard Roberts, Jeffrey Elsner, and Martha W. Bagnall. Delayed otolith development does not impair vestibular circuit formation in zebrafish. *Journal of the Association for Research in Otolaryngology*, 18(3):415–425, March 2017.

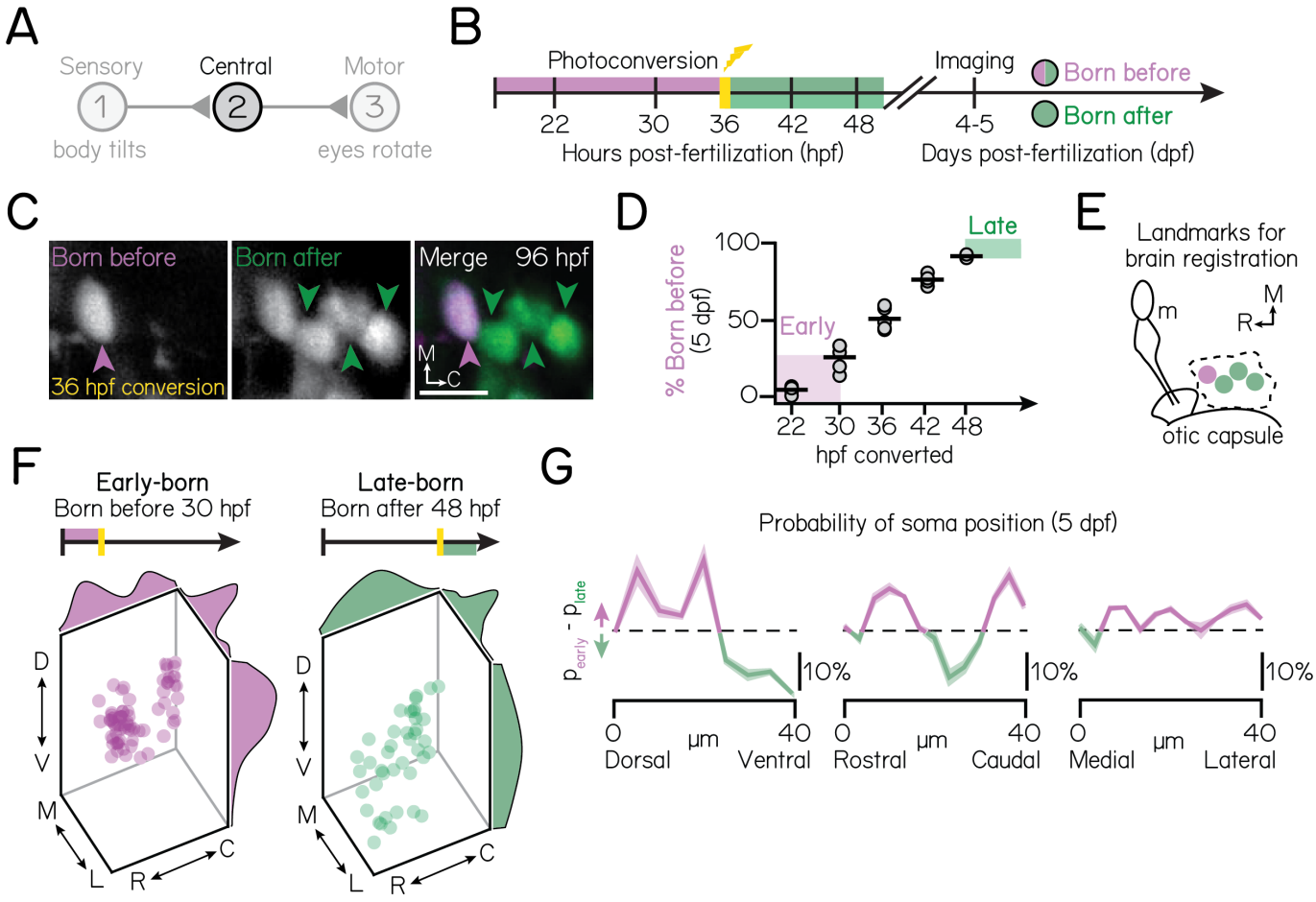

Figure 1: Projection neuron birthdate predicts soma position. (A) Schematic of the vestibulo-ocular reflex circuit used for gaze stabilization. **(B)** Timeline of photoconversion experiments. Neurons born by the time of photoconversion have both magenta (converted) and green (unconverted) Kaede. Neurons born after photoconversion have exclusively green (unconverted) Kaede. All fish are imaged well after photoconversion, at 96-120 hours post-fertilization (hpf) **(C)** Example projection neurons photoconverted at 36 hpf. Magenta and green arrows indicate neurons born before or after 36 hpf, respectively. Scale bar (white) is 20 μm. **(D)** Percent of projection neurons born at each timepoint. Black lines indicate the mean percent across individual fish (circles). Shaded bars indicate neurons in the early- (born before 30 hpf) or late-born (born after 48 hpf) cohorts. n=5 hemispheres/timepoint from at least N=3 larvae (22-42 hpf) or n=3 hemispheres from N=3 larvae (48 hpf). **(E)** Schematic of brain registration method. Solid lines outline anatomical landmarks used for registration. Black dotted line outlines tangential nucleus. m, Mauthner neuron. **(F)** Soma position of early- and late-born projection neurons. Marginal distributions illustrate the probability of soma position in each spatial axis. Early-born: n = 74 neurons from N = 7 fish. Late-born: n = 41 neurons from N = 10 fish. **(G)** Probability of soma position in each spatial axis, shown as the difference between the probability distributions of early- and late-born soma. Regions above the black dashed line indicate a higher probability of early-born soma; below the line, late-born soma. Solid lines shows mean from jackknife resampling; shaded bars, standard deviation.

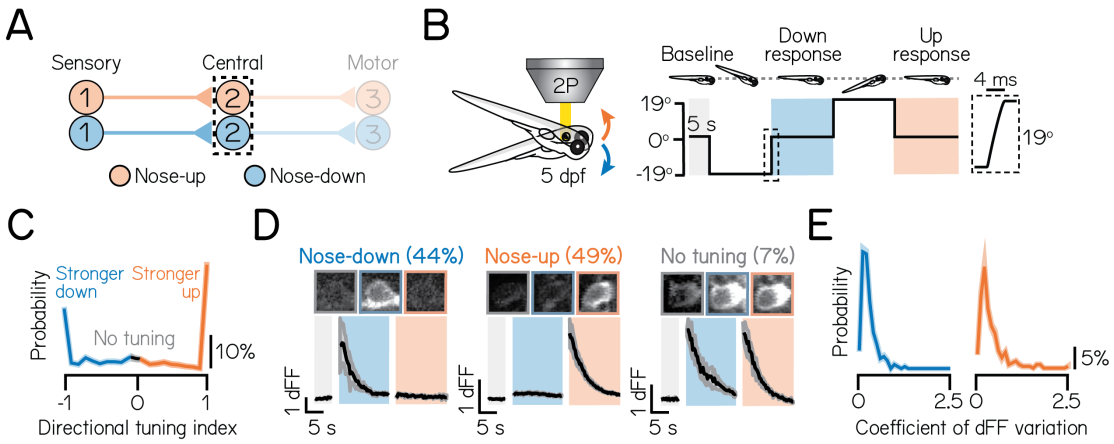

Figure 2: Pitch-tilt rotations reliably differentiate two cardinal subtypes of projection neurons. (A) Circuit schematic for pitch-tilt rotation experiments. Black dashed lines outline projection neurons as circuit population of focus. **(B)** Pitch-tilt rotation stimulus. Left: Schematic of imaging paradigm. Right: Stimulus waveform. Shaded bars show time at the horizontal imaging plane. Dotted box shows zoom of restoration step to horizontal. **(C)** Probability distribution of the directional tuning for all sampled neurons. Grey region indicates neurons with no directional tuning; blue and orange regions indicate neurons with stronger nose-down or nose-up responses, respectively. Criteria detailed in Methods. Solid line shows mean from jackknife resampling; shaded bars, standard deviation. **(D)** Example traces from a nose-down neuron (left), nose-up neuron (middle), and a neuron with no directional tuning. Black line shows mean response; grey shaded lines are the standard deviation across trials. Parentheses indicate percent of neurons with each subtype, n = 467 neurons, N = 22 fish. **(E)** Probability distributions of the coefficient of variation for the maximum dFF response across three trials for nose-down (left) and nose-up (right) neurons. Solid lines shows mean from jackknife re-sampling; shaded bars, standard deviation.

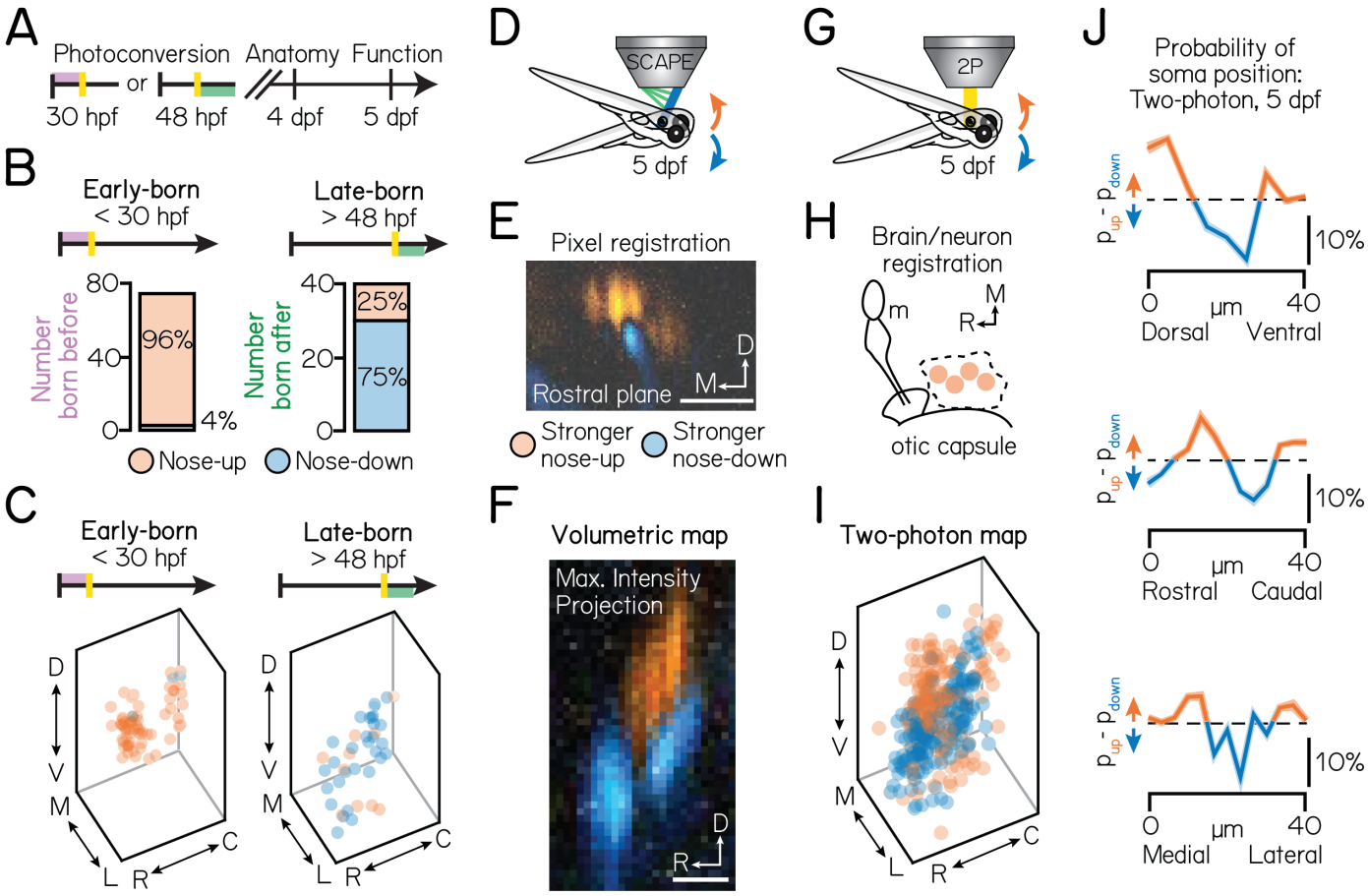

Figure 3: Birthdating reveals functional somatic topography to projection neurons. (A) Schematic of birthdating experiments. Larvae are birthdated at either 30 hpf or 48 hpf and then imaged on a confocal (4 dpf) and two-photon (5 dpf) to identify projection neuron soma position and directional tuning. **(B)** Number of early- (left) and late-born (right) projection neurons with each directional subtype identity. Data from same neurons shown in Figure 1. **(C)** Soma position of early- (left) and late-born (right) neurons, pseudocolored according to directional tuning. **(D)** Schematic of volumetric imaging paradigm with swept, confocally-aligned planar excitation (SCAPE) microscopy. Larvae are presented with the same pitch-tilt stimulus as in Figure 2A. **(E)** Registration method. Pixels are pseudocolored according to the direction that evoked a stronger response. One example rostral plane shown. **(F)** Three-dimensional maximum intensity projection of the entire tangential nucleus from one fish. Pixels pseudocolored as described in D. **(G)** Schematic of planar two-photon imaging paradigm, as described in Figure 2. **(H)** Schematic of brain and neuron registration method using the anatomical landmarks shown in Figure 1E. **(I)** Soma position of all neurons, pseudocolored according to directional tuning. Data from the same n=467, N = 22 fish as in Figure 2. **(J)** Probability of up/down soma position in each spatial axis, shown as the difference between the probability distributions of the nose-up and nose-down neurons shown in panel I. Regions above the black dashed line indicate a higher probability of nose-up soma; below the line, nose-down soma. Solid lines shows mean from jackknife resampling; shaded bars, standard deviation. All scale bars (white) are 20 μm.

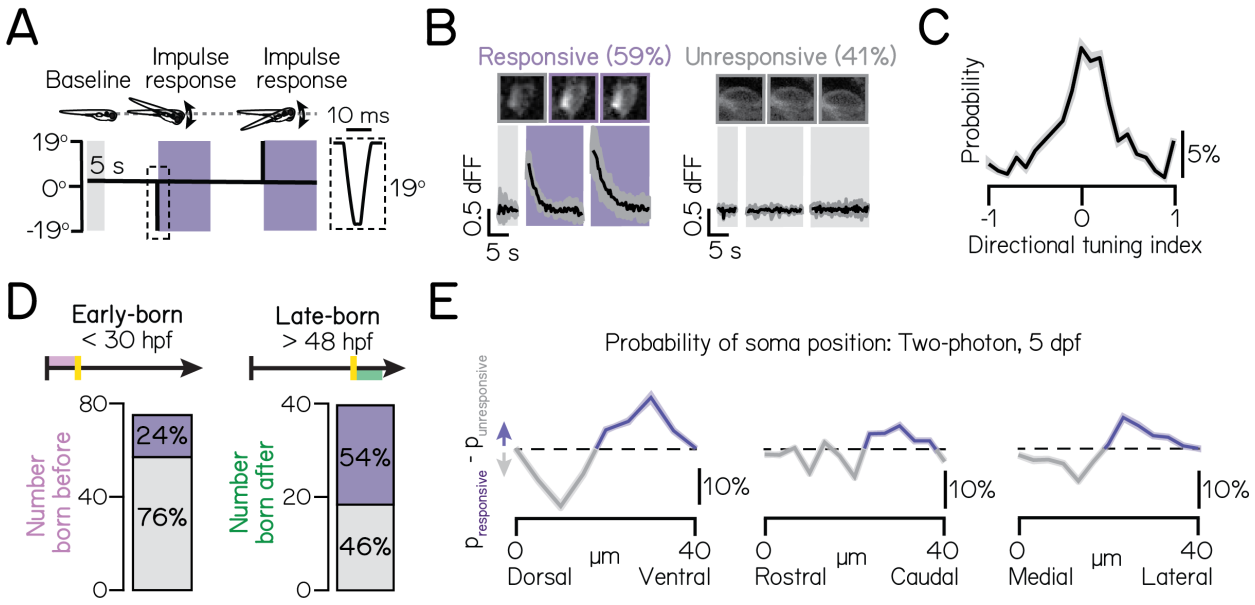

Figure 4: Birthdate reveals somatic topography to high-frequency stimulation sensitivity in projection neurons. **(A)** Impulse stimulus waveform. Shaded bars indicate time in the horizontal imaging plane, where calcium activity is measured. Dotted box shows zoom of 10 ms impulse. **(B)** Example traces from an impulse-responsive projection neuron (left) and an unresponsive neuron (right). Parenthesis show percent of responsive and unresponsive neurons. n = 467 neurons, N = 22 fish. **(C)** Probability distribution of the directional preference strength to impulse rotations. Zero indicates no directional preference. Solid lines shows mean from jackknife resampling; shaded bars, standard deviation. **(D)** Number of early- and late-born projection neurons with impulse responses (purple) or no impulse responses (grey). Data from same fish as in Figure 1F-1G. **(E)** Probability of soma position in each spatial axis, shown as the difference between the probability distributions of impulse-responsive and impulse-unresponsive neurons. Regions above the black dashed line indicate a higher probability of impulse-responsive soma; below the line, impulse-unresponsive soma. Data from the same neurons shown in Figure 3I-3J. Solid lines shows mean from jackknife resampling; shaded bars, standard deviation.

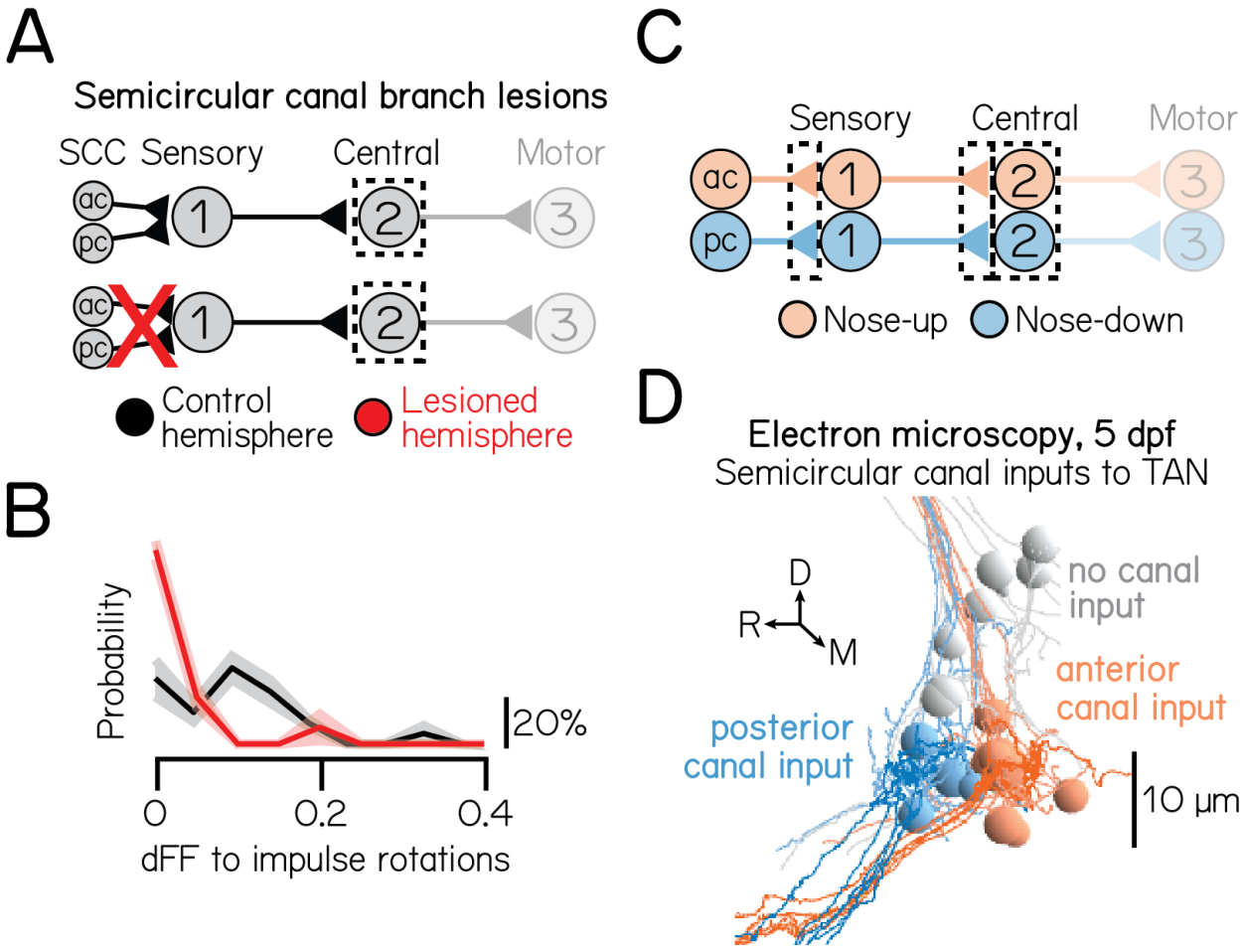

Figure 5: Semicircular canal inputs mediate high-frequency stimulation responses and are topographically organized. (A) Circuit schematic. Both the anterior and posterior semicircular canal branches of the VIIIth nerve are unilaterally lesioned. Calcium responses of projection neurons (black dashed box) in lesioned and control hemispheres are compared. **(B)** Probability distributions of the maximum dFF response to impulse rotations in lesioned (red) and control (black) hemispheres. Responses shown only for the most ventral 15µm of projection neurons. Solid lines shows mean from jackknife resampling; shaded bars, standard deviation. Control: n = 68 impulse responses, N = 3 fish. Mutants: n = 132 impulse responses, N = 3 fish. **(C)** Circuit schematic for electron microscopy experiments. Black dashed lines indicate the circuit elements of focus: synaptic connections from the anterior and posterior semicircular canals to first-order sensory neurons, synaptic connections from sensory neurons to projection neurons, and the projection neurons. **(D)** Electron microscopy reconstruction of 19 projection neurons at 5 dpf. Soma pseudocolored based on innervation from sensory neurons that receive anterior semicircular canal input (orange) or posterior semicircular canal input (blue). Grey soma receive no semicircular canal input.

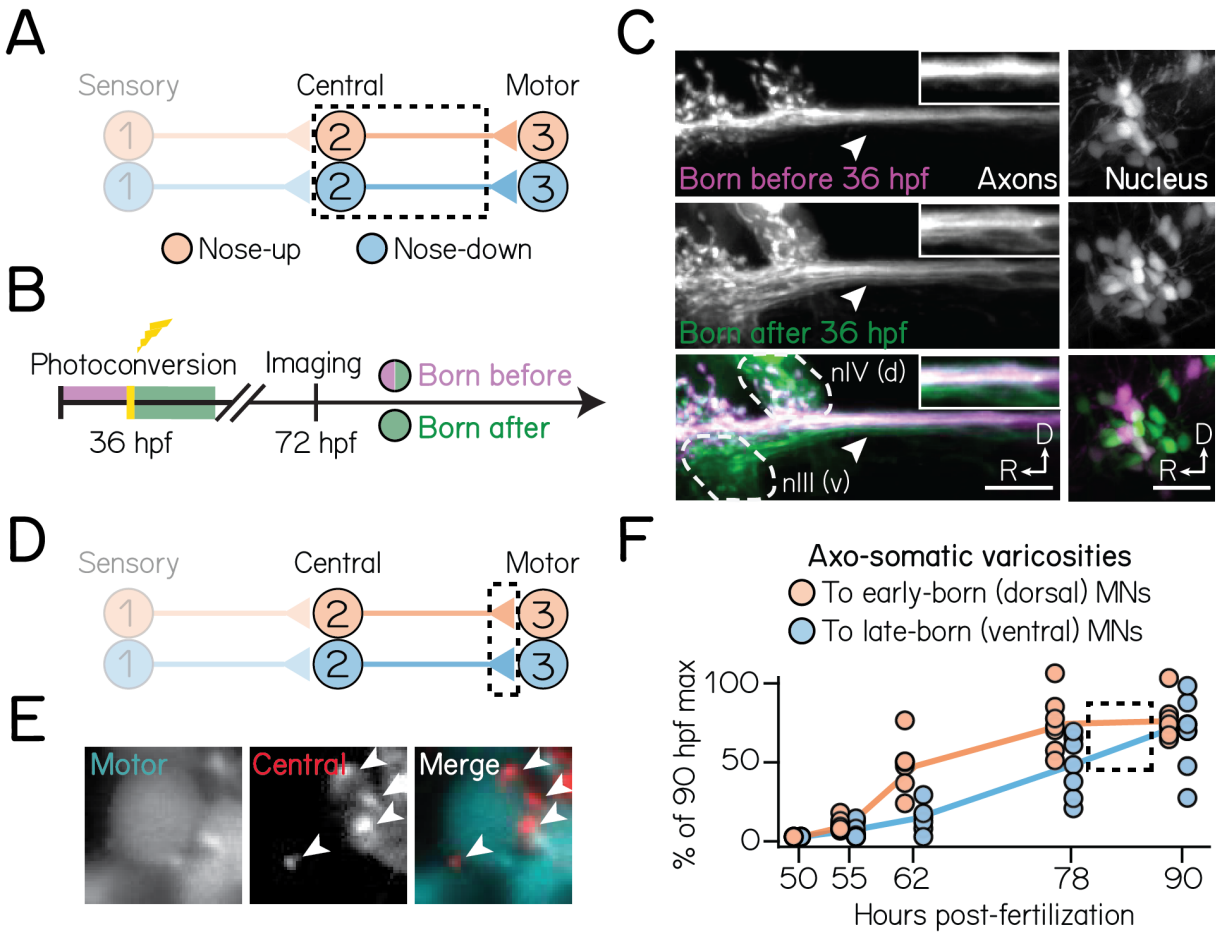

Figure 6: Birthdate predicts patterns of axonal trajectories and synapse formation between projection neurons and extraocular motor neurons. (A) Circuit schematic for axon birthdating experiments. Black dashed lines outline projection neuron soma and axonal projections to the extraocular motor nuclei. **(B)** Timeline of axon birthdating experiments. Larvae are only photoconverted at 36 hpf. **(C)** Birthdated axons from one example fish. Top row shows axons (left) from soma (right) born by 36 hpf; middle row shows axons that were not born by 36 hpf; bottom row shows merge. White arrows point to the ventral axon bundle. Inset shows zoom of axons. Dotted lines outline extraocular motor neuron somata. Scale bars, 20 μm. **(D)** Circuit schematic for synapse formation measurements. Black dashed lines outline axo-somatic varicosities from projection neurons onto post-synaptic ocular motor neurons. **(E)** Example image of an extraocular motor neuron (left) and axo-somatic varicosities (middle); right image shows merge. White arrows point to four example varicosities. Scale bar, 5 μm **(F)** Rate of varicosity growth to early- and late-born ocular motor neurons, quantified as as a percentage of the maximum number of varicosities observed at 90 hpf. Circles represent individual fish. Dotted box highlights the time where the rate of varicosity formation to motor neuron subtypes diverges. n ≥ 5 fish per timepoint.

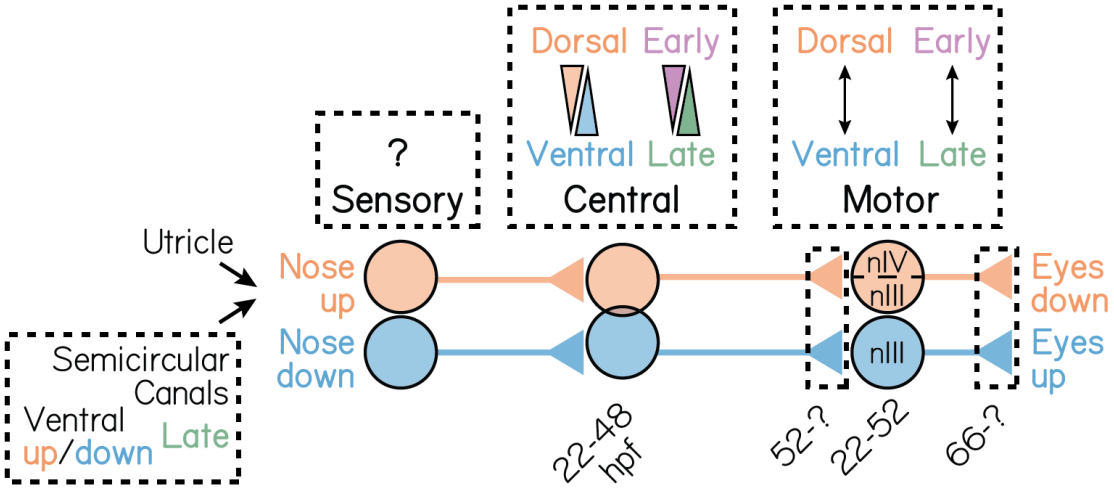

Figure 7: A model for the spatiotemporal organization of the gaze stabilization circuit. Spatiotemporal development of neurons that mediate the nose-up/eyes-down (orange) and nose-down/eyes-up (blue) gaze stabilization reflexes. nIII refers to the oculomotor cranial nucleus; nIV to the trochlear cranial nucleus IV.

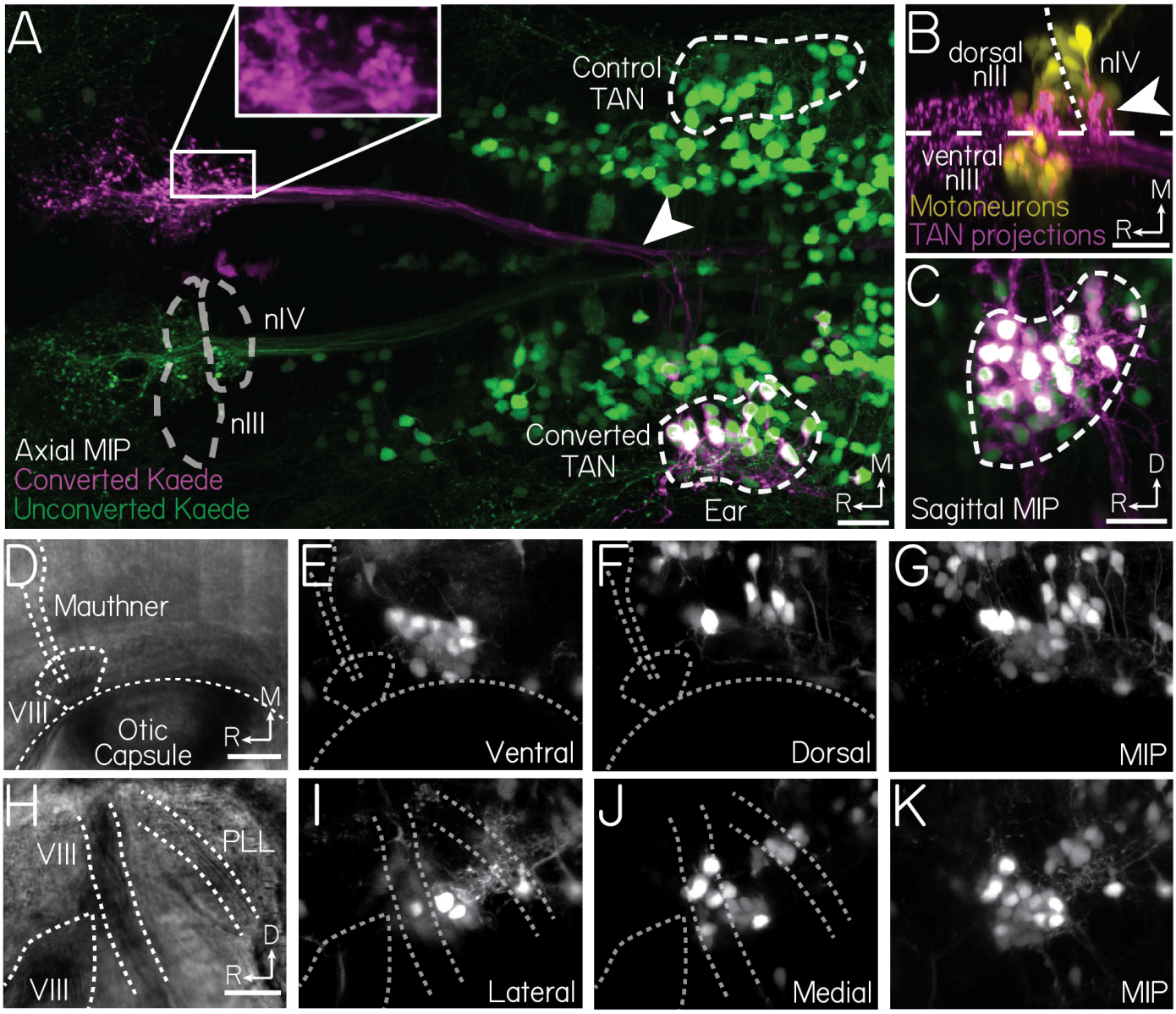

Figure S1: Localization of the tangential vestibular nucleus. (A) Retrograde photofill technique. Maximum intensity projection (MIP) of the tangential vestibular nucleus and its ascending projections at 5 dpf. White box shows conversion target region. White arrow points to ascending projections. Grey dashed lines outline the position of the extraocular motor nuclei. White dashed lines outline the bounds of photofilled soma in the tangential vestibular nucleus. **(B)** Photoconversion target region. White arrow points to the characteristic axonal arborizations at cranial nucleus IV (nIV). Motor neurons labeled in yellow. Ascending projections labeled in magenta. Horizontal dashed line indicates midline. Diagonal white dashed line shows midbrain-hindbrain boundary. **(C)** Center-surround appearance of converted (magenta) and unconverted (green) Kaede in retrogradely-labeled soma. **(D-G)** Location of the tangential vestibular nucleus in an axial view. **(D)** Transmitted light view of the tangential vestibular nucleus, 15 µm ventral to the base. Grey dashed lines outline the otic capsule, VIIIth cranial nerve, and lateral dendrite of the Mauthner neuron. **(E)** Ventral plane, approximately 15 µm dorsal to the base. Landmarks in D labeled as grey dashed lines. **(F)** Dorsal plane, approximately 35 µm dorsal to the base. **(G)** Maximum intensity projection. **(H-K)** Location of the tangential vestibular nucleus in a sagittal view. **(H)** Transmitted light view, 10 µm from the lateral edge. White dashed lines outline the entry point and ascending branch of the VIIIth nerve (VIII) and the posterior lateral line branch (PLL). **(I)** Lateral plane, approximately 10 µm medial to the lateral edge. **(J)** Medial plane, approximately 30 µm medial to the lateral edge. **(K)** Maximum intensity projection. All scale bars 20 µm.

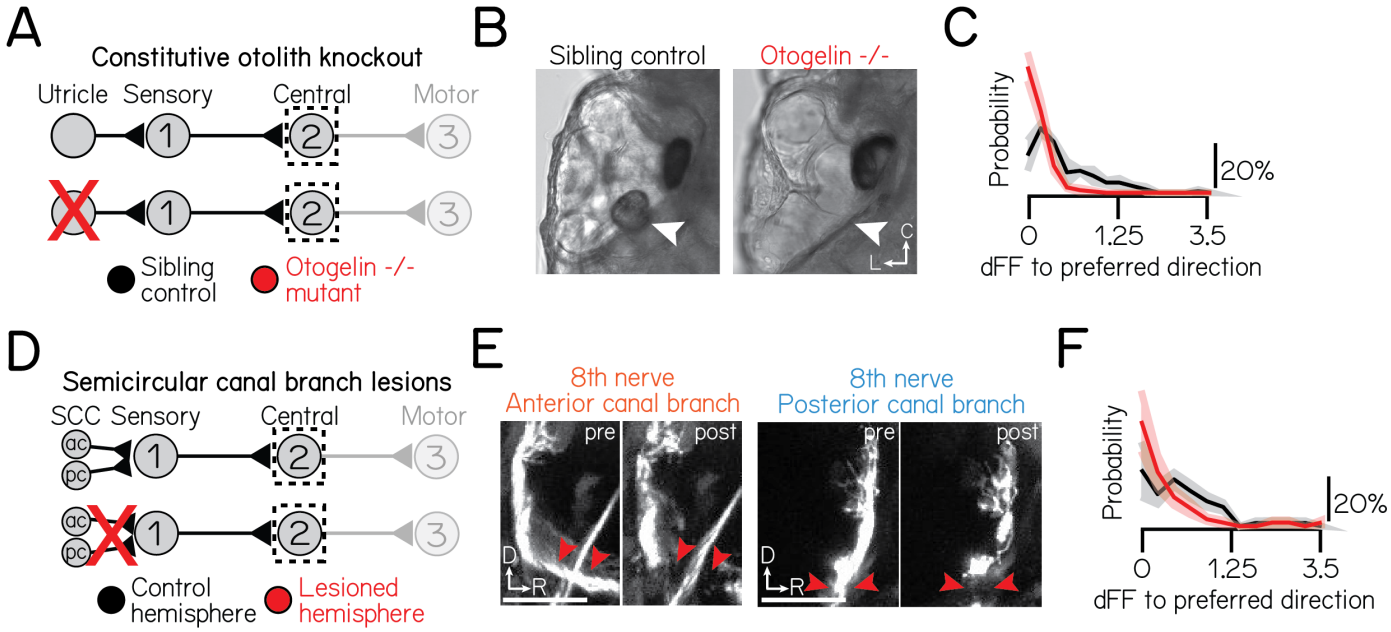

Figure S2: Responses to tonic pitch-tilt rotations originate primarily from the utricular otoliths. **(A)** Circuit schematic for utricular otolith knockout experiments. Black dashed lines outline the tangential nucleus as the circuit element of focus. **(B)** Example images from a control larvae (left) and an otogelin null mutant (right). White arrow points to the position of the utricular otolith. **(C)** Probability distributions of the maximum dFF response to preferred directional pitch-tilts in control (black) and otogelin mutants (red). Solid lines shows mean from jackknife resampling; shaded bars, standard deviation. Controls: n = 144 neurons, N = 3 fish; Mutants: n = 183 neurons, N = 3 fish. **(D)** Circuit schematic for uni-lateral VIIIth nerve lesions (anterior and posterior semicircular canal branches). **(E)** Example images from larvae before and after uni-lateral VIIIth nerve lesions. Left and right image sets show the anterior and posterior semicircular canal branches, respectively, before and after lesion. Both branches are lesioned in each experiment. Red arrows point to lesion sites. **(F)** Probability distributions of the maximum dFF response to preferred directional pitch-tilts in control (black) and lesioned (red) hemispheres.Solid lines shows mean from jackknife resampling; shaded bars, standard deviation. Control hemisphere: n = 57 neurons, N = 4 fish; Lesioned hemisphere: n = 49 neurons, N = 4 fish. All scale bars, 20 μm.

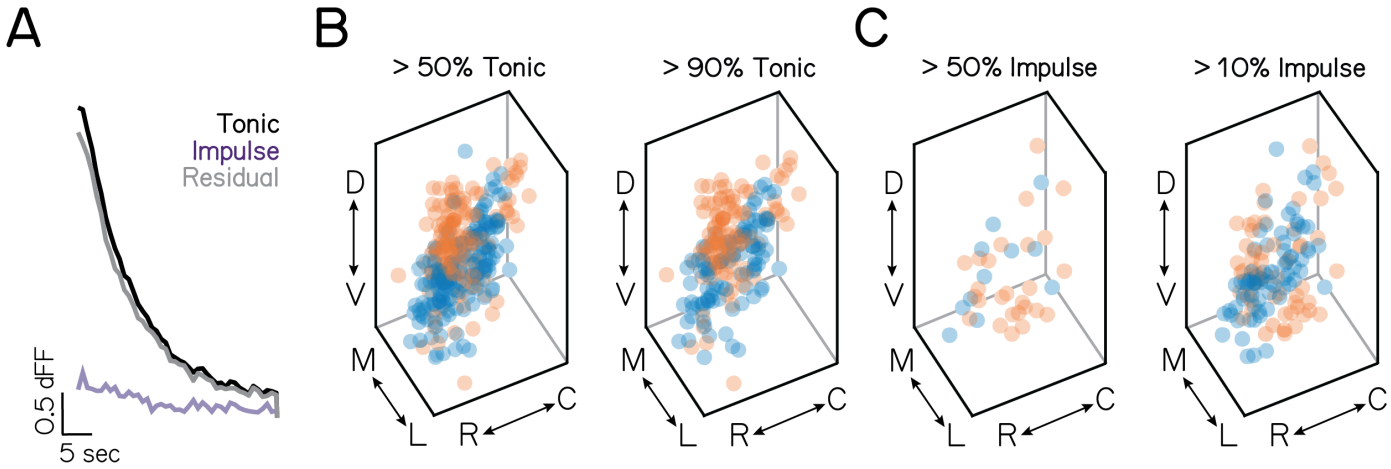

Figure S3: The spatial organization of tonic nose-up/nose-down subtypes remains constant when controlling for impulse responses. (A) Subtraction method. Impulse responses are subtracted from tonic responses to generate a residual. **(B)** Soma position of nose-up (orange) and nose-down (blue) neurons where the tonic response comprised at least 50% (left) or 90% (right) of the total. **(C)** Soma position of nose-up and nose-down neurons where the impulse response comprised at least 50% (left) or 10% (right) of the total.

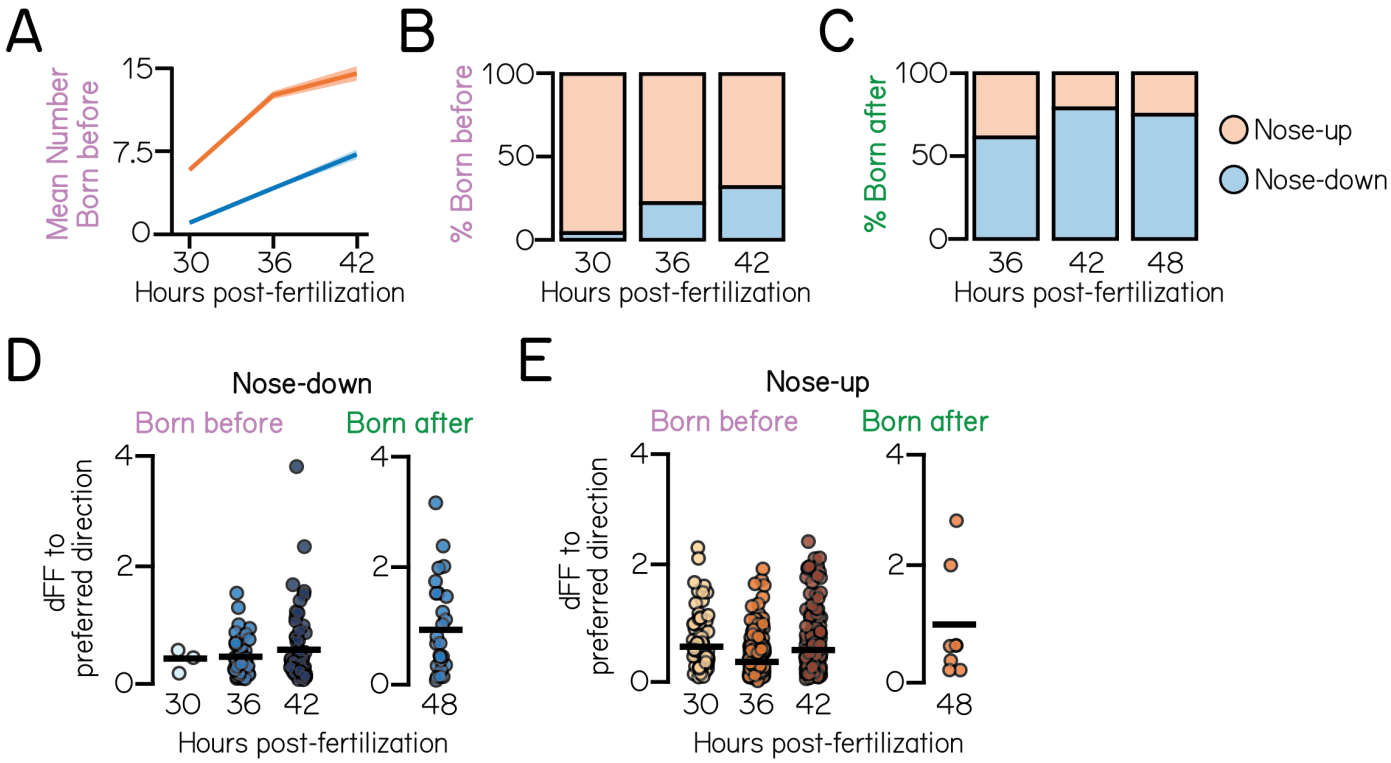

Figure S4: Neuronal birthdate predicts nose-up/nose-down selectivity, but not response strength to tilts. (A) Mean number of nose-up and nose-down neurons born before (converted Kaede) each age. Solid and shaded lines show the mean and standard deviation, respectively, after jackknife resampling. Orange, nose-up; blue, nose-down. 30 hpf data is from the same N=7 fish as in Figure 1F and Figure 3B-C. 36 hpf: n=208 sampled "born before" neurons from N=7 fish; 42 hpf: n=198 sampled "born before" neurons from N=5 fish. **(B)** Percent of sampled nose-up and nose-down neurons born before each age. **(C)** Percent of nose-up and nose-down neurons born after (unconverted Kaede) each age. 36 hpf: n=168 "born after" neurons from N=7 fish; 42 hpf: n=66 "born after" neurons from n=5 fish. 48 hpf data same as in Figure 1F and Figure 3B-C. **(D)** Maximum change in calcium fluorescence to tonic tilts for nose-down neurons born before (left) or after (right) each age. Each circle represents a unique cell. Solid line shows the mean across cells.

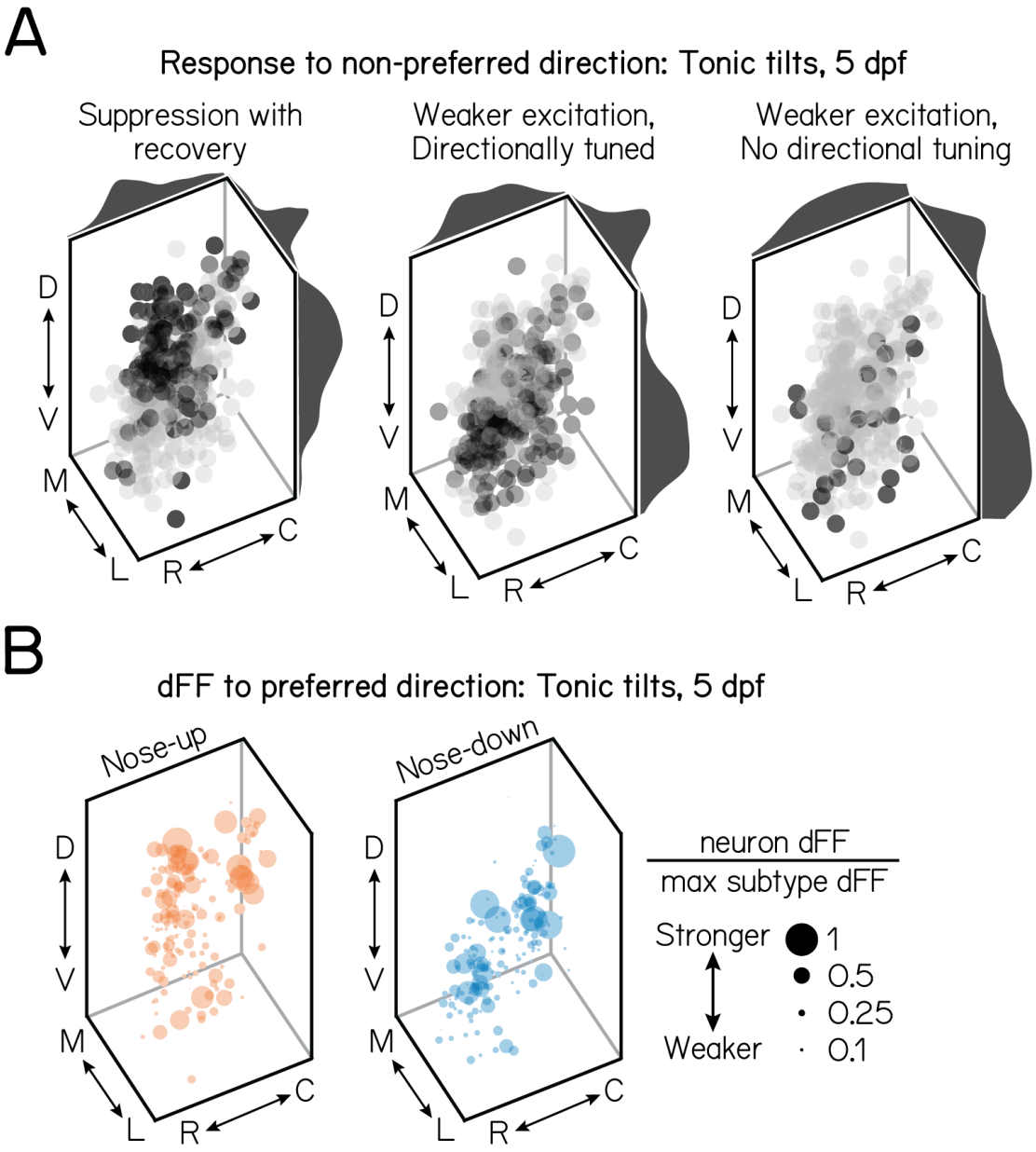

Figure S5: Projection neuron soma are locally organized according to similarities in tilt responses. (A) Soma position of projection neurons with each type of response to their non-preferred, tonic tilt direction. Dark grey shows neurons with the given response; light grey shows all other neurons. The directional tuning of neurons with weak excitation to non-preferred directions is determined by their directional tuning index (> 0.1 or ≤ 0.1). Marginal distributions illustrate the probability of soma position in each spatial axis. Data from the same neurons shown in Figure 3I. **(B)** Soma position of nose-up (left) and nose-down (right) projection neurons, scaled according to the strength of their calcium response (dFF) to tilts relative to the strongest response observed for that subtype. Larger circles indicate stronger responses. Data from the same neurons shown in Figure 3I.

Afferent source	1	2	3	4	5	6	7	8	9	10	11	12	13	14	15	16	17	18	19	Tuning
Ear_AnteriorCrista_R_01	0	0	0	0	0	0	0	0	0	0	0	0	8	0	0	0	0	0	0	
Ear_AnteriorCrista_R_02	0	0	0	0	**2**	0	0	0	0	0	0	0	0	**8**	0	0	0	0	0	
Ear_AnteriorCrista_R_03	0	0	0	0	0	0	0	0	**3**	0	0	0	0	0	0	0	0	0	0	
Ear_AnteriorCrista_R_04	0	0	0	0	**1**	0	0	0	0	0	0	**9**	0	0	0	0	0	0	0	
Ear_AnteriorCrista_R_05	0	0	0	0	0	0	0	0	**2**	0	0	0	0	0	0	0	0	0	**12**	
Ear_AnteriorCrista_R_06	0	0	0	0	0	0	0	0	**5**	0	0	0	0	0	0	0	0	0	0	
Ear_PosteriorCrista_R_01	0	0	0	0	0	0	0	0	0	0	0	0	0	0	0	0	0	0	0	
Ear_PosteriorCrista_R_02	0	0	0	0	0	**2**	0	0	0	**2**	0	0	0	0	0	0	**8**	0	0	
Ear_PosteriorCrista_R_03	0	0	0	0	0	0	0	0	0	0	0	0	0	0	0	0	0	**7**	0	
Ear_PosteriorCrista_R_04	0	0	0	0	0	**3**	0	0	0	**1**	0	0	0	0	**10**	0	0	0	0	
Ear_PosteriorCrista_R_05	0	0	0	0	0	0	0	0	0	**1**	0	0	0	0	0	**5**	0	0	0	
Ear_AnteriorMacula_R_01	**1**	0	**2**	**3**	0	0	0	0	0	0	0	0	0	0	0	0	0	0	0	6.00894
Ear_AnteriorMacula_R_02	0	**3**	0	0	0	0	0	0	0	0	0	0	0	0	0	0	0	0	0	6.09989
Ear_AnteriorMacula_R_03	**1**	0	0	0	0	0	0	0	0	0	0	0	0	0	0	0	0	0	0	6.08107
Ear_AnteriorMacula_R_04	0	**3**	**1**	0	0	**1**	0	0	0	0	0	0	0	0	0	0	0	0	0	5.92756
Ear_AnteriorMacula_R_05	0	0	0	0	0	0	**1**	0	0	0	0	0	0	0	0	0	0	0	0	0.204992
Ear_AnteriorMacula_R_06	**1**	0	0	0	**1**	0	**1**	0	0	0	0	0	0	0	0	0	0	0	0	0.523691
Ear_AnteriorMacula_R_07	0	0	0	**1**	0	0	0	0	0	0	0	0	0	0	0	0	0	0	0	0.825107
Ear_AnteriorMacula_R_08	0	0	0	0	**1**	0	0	0	0	0	**1**	0	0	0	0	0	0	0	0	1.37515
Ear_AnteriorMacula_R_09	**1**	0	**4**	0	0	0	0	0	0	0	0	0	0	0	0	0	0	0	0	6.04532
Ear_AnteriorMacula_R_10	0	0	0	0	0	0	0	0	0	0	0	0	0	0	0	0	0	0	0	1.21203
Ear_AnteriorMacula_R_11	0	0	0	0	0	0	0	0	0	0	0	0	0	0	0	0	0	0	0	4.20026
Ear_AnteriorMacula_R_12	0	0	0	**2**	0	0	0	**2**	0	0	0	0	0	0	0	0	0	0	0	1.61526
Ear_AnteriorMacula_R_13	0	0	0	0	0	0	**1**	0	0	0	0	0	0	0	0	0	0	0	0	0.257178
Ear_AnteriorMacula_R_14	0	0	0	0	0	0	0	0	0	0	0	0	0	0	0	0	0	0	0	3.09177
Ear_AnteriorMacula_R_15	0	0	0	0	0	0	0	**2**	0	0	0	0	0	0	0	0	0	0	0	0.93221
Ear_AnteriorMacula_R_16	0	0	0	0	0	0	0	0	0	0	0	0	0	0	0	0	0	0	0	4.19152
Ear_AnteriorMacula_R_17	0	0	0	0	0	0	**1**	0	0	0	0	0	0	0	0	0	0	0	0	1.31298

Table 1: Table 1: Number of synapses between 28 VIIIth nerve afferents and 19 projection neurons